# CFD Uncertainty Quantification using Stochastic Spectral Methods - Exemplary Application to a Buoyancy-Driven Mixing Process

Philipp J. Wenig [a], Stephan Kelm [b], Markus Klein [a]

[a] *Institute of Applied Mathematics and Scientific Computing, University of the Bundeswehr Munich, Werner-Heisenberg-Weg 39, 85577 Neubiberg, Germany*
[b] *Institute of Energy and Climate Research, Forschungszentrum Jülich GmbH, 52425 Jülich, Germany*

**Abstract**

The consideration of uncertainties is of particular importance for nuclear reactor safety, where high safety standards for example ensure the integrity of the containment. By means of Computational Fluid Dynamics (CFD), buoyancy-induced mixing processes, which can take place during a severe reactor accident, are investigated. However, the CFD models contain uncertainties, which have a large impact on the present flow and have to be analyzed. The method development for the subsequent Uncertainty Quantification of a representative reactor test containment is conducted using the Differentially Heated Cavity of aspect ratio 4 with $Ra = 2 \times 10^9$ as a generic test case from the literature. In this way, methods for the future quantification of uncertainties in large-scale industrial applications are established. Results from single-fidelity models such as Unsteady Reynolds-Averaged Navier-Stokes, Large Eddy Simulation and Direct Numerical Simulation are presented and combined to three-level multifidelity models. Stochastic representations of scalar random responses are constructed by means of Polynomial Chaos Expansions and Karhunen-Loève Expansions are derived for the representation of stochastic processes. A new approach for the description of highly dynamic transient processes called Random Field Composi-

*Corresponding author.
*Email address:* philipp.wenig@unibw.de (Philipp J. Wenig )

tion (RFC) is presented, which proposes stochastic model construction through combination of multiple random fields. The presented multifidelity (MF) models achieve high accuracy in combination with a justifiable computational effort. Therefore, MF modeling serves as a promising approach for large-scale applications. Furthermore, it is found, that RFC allows for the description of highly dynamic processes with a reasonable number of simulation runs, if the complexity of the stochastic process representation can be reduced by partitioning the stochasticity into single random fields.

*Keywords:* Uncertainty Quantification, Buoyancy-driven transient mixing process, Polynomial Chaos Expansion and Karhunen-Loève Expansion, Random Field Composition, Error estimation, Variance-based decomposition

## 1. Introduction

Computational models enable predictions in the design process of technical components in mechanical or plant engineering and allow for the adaptation to subsequent application requirements. However, predictions based on numerical models are subject to uncertainties, due to unknown or imprecise input parameters, mathematical models or approximations and numerical methods. In some applications, these uncertainties can have a large impact on the results, which the model is supposed to predict. The high complexity of computational models in the field of nuclear reactor safety leads to considerable uncertainties, which might have significant influence on the results. One example is the prediction of flow phenomena by means of CFD. Since the prevention of the release of radioactive substances has to be ensured, numerical simulations are conducted for the prediction of hydrogen distribution and pressure build-up in a nuclear reactor containment during an accident scenario [1, 2]. The formation, stability, as well as the remobilization of a locally flammable gas layer have been studied with CFD and experiments. However, CFD analysis for the reproduction of natural convection experiments like MISTRA NATHCO [3] (CEA, France) and THAI-TH22 [4] (Becker Technologies, Germany) have shown that the specified initial

and boundary conditions [5] (e.g., initial gas and wall temperatures) have a major influence on the results. In addition, the specification of initial and boundary conditions within the CFD simulation is subject to uncertainty, which is due to missing input variables or measurement inaccuracies [6, 7]. Consequently, results are also subject to uncertainties, which have to be taken into account. For their evaluation though, insufficient experience exists [8, 9]. Therefore, the present work presents promising methodologies for the Uncertainty Quantification (UQ) of buoyancy-driven flows and mixing processes. As preparation for the later UQ analysis of the THAI-TH32 experiment [10], the method development is first conducted using a generic test case from the literature, which reflects similar physics as those expected inside the reactor test containment of the THAI test series. The initial application to a simplified configuration allows for testing of existing methods and their further development at a reasonable computational cost. As a test case, the Differentially Heated Cavity (DHC) with aspect ratio 4 [11, 12, 13] was chosen and extended to a superimposed mixing process. It is a tall cavity with hot left wall and cold right wall, in which natural convection flow and buoyancy-induced mixing processes occur in the presence of two gas mixtures with different densities.

In the following, a brief summary of related UQ studies, which are reported in the literature, is provided. Single-phase mixing within a flow channel was investigated in [14, 15, 16, 17, 18]. Two parallel streams with different densities, which are initially separated by a splitter plate, are mixed under turbulent conditions. These studies analyzed discrete random field data by means of Polynomial Chaos Expansions (PCE) and results were compared with experimental data. Thermo-fluid flow within the DHC was studied by Le Maître et al. in the Boussinesq [19] and non-Boussinesq limits [20] through solving the low-Mach-number equations. Uncertainties in the mean velocity field, which originate from the uncertain cold wall temperature, were investigated in a discrete manner using PCE. Impact of uncertainty in heated bottom wall temperature for Rayleigh–Bénard convection (RBC) was considered using PCE in [21]. Further advanced UQ methodologies were applied to different areas in the field of

CFD. Uncertainty quantification of the performance of a sailing yacht hull was conducted using multifidelity kriging or gaussian process modeling by de Baar et al. [22]. Later, the methodology was extended to an adaptive multifidelity Kriging approach, which was applied to CFD of an axial compressor rotor test case [23]. Palar et al. enhanced multifidelity Kriging through the utilization of PCE and evaluated the method using different test problems [24]. Uncertainties in the CFD simulation of turbine blade leading edge film cooling were assessed by Mohammadi-Ahmar et al. [25] using bi-fidelity models, which were determined from PCEs based on the Orthogonal Matching Pursuit (OMP) and the Kriging method. Multifidelity PCEs were also successfully applied to UQ of film cooling flow under random operational and geometrical conditions by Mohammadi-Ahmar et al. [26]. Furthermore, Uncertainty Quantification also established in aerospace engineering for the assessment of predictions in the field of CFD. Huan et al. [27] studied uncertain spatially dependent fields using Karhunen-Loève Expansions (KLE), which allows for the continuous description of random fields, for further development of scramjet engines along with efficient and stable propulsion under hypersonic flight conditions. A turbulent round jet was analyzed in a similar fashion by Jivani et al. [28] using KLE in conjunction with PCE. The approach was extended to multifidelity modeling in order to create stochastic models of high accuracy with justifiable computational cost.

The present research transfers promising methods to the field of nuclear reactor safety and continues the work of Wenig et al. [29] in the field of uncertainty quantification for buoyancy-induced turbulent mixing processes between two miscible fluids within the DHC. The results comprise the presentation of scalar integral quantities and time-dependent stochastic processes, which are approximated through Polynomial Chaos Expansions and Karhunen-Loève Expansions. Single-fidelity CFD models, such as Unsteady Reynolds-Averaged Navier-Stokes (URANS), Large Eddy Simulation (LES) and Direct Numerical Simulation (DNS) , are considered and combined to multifidelity models. In addition, a new approach to describe stochastic processes is presented, which proposes the coupled representation of stochastic processes through function

composition of single random fields, referred to as Random Field Composition. When using this method, highly dynamic transient processes are represented through partitioning stochasticity into single less complex random fields. Furthermore, single-fidelity and multifidelity results are compared with stochastic models from DNS, variance fractions are attributed to uncertain input variables by determination of total-order Sobol indices and error estimates are calculated, which indicate potential model improvement and localize possible model deficiency. Through the evaluations, the developed techniques are proven an appropriate methodology for the future uncertainty quantification of the THAI-TH32 experiment.

The paper is structured as follows. Section 2 covers the methods, which were used for the prediction and stochastic representation of the underlying flow phenomena. Afterwards the obtained results are presented and discussed in Section 3. A summary of the work and of important findings is provided in Section 4.

## 2. Methods

In Section 2.1, mathematical models and numerical techniques to predict the underlying fluid flow are presented. Details about the applied stochastic spectral methods for the UQ analysis are provided in Section 2.2.

### *2.1. Computational Fluid Dynamics*

The governing equations are introduced in Section 2.1.1. This is followed by the description of the case setup in Section 2.1.2 and the numerical framework along with the discretization in Section 2.1.3.

#### *2.1.1. Governing Equations*

For the subsequent CFD analysis, low Mach number flow of two Newtonian viscous fluids is considered. The modelled governing equations for continuity,

momentum, energy, and species transport take the form (for simplicity the averaging or filtering operations are omitted)

$$
\begin{aligned}
&\frac{\partial \rho}{\partial t} + \nabla \cdot (\rho \mathbf{u}) = 0, \\
&\frac{\partial \rho \mathbf{u}}{\partial t} + \nabla \cdot (\rho \mathbf{u}\mathbf{u}) = -\nabla p + \rho \mathbf{g} + \nabla \cdot (2\mu_{eff}\, \tau(\mathbf{u})) - \nabla \cdot \left( \frac{2}{3} \mu_{eff} (\nabla \cdot \mathbf{u}) \right), \\
&\frac{\partial \rho h}{\partial t} + \frac{\partial \rho K}{\partial t} + \nabla \cdot (\rho \mathbf{u} h) + \nabla \cdot (\rho \mathbf{u} K) - \frac{\partial p}{\partial t} = \nabla \cdot (\rho \alpha_{eff} (\nabla h)) + \rho \mathbf{u} \cdot g + S_D, \\
&\frac{\partial \rho Y_i}{\partial t} + \nabla \cdot (\rho \mathbf{u} Y_i) = \nabla \cdot (\rho D_{eff} (\nabla Y_i)), \qquad (1)
\end{aligned}
$$

where $\mathbf{u}$ is the velocity field, $\rho$ is the density field, $p$ is the static pressure field, $\mathbf{g} = (0, g, 0)$ is the gravitational acceleration vector, $h$ is the enthalpy, $K = \frac{1}{2} |\mathbf{u}|^2$ is the kinetic energy of the system, $Y_i$ is the mass fraction of the $i$th species from the set of gas species indices given by $N = \{1, 2\}$, and the rate of strain tensor is defined as $\tau(\mathbf{u}) = \frac{1}{2} \left( \nabla \cdot \mathbf{u} + (\nabla \cdot \mathbf{u})^T \right)$. $S_D$ accounts for the enthalpy transport due to diffusive mass transport and the associated correction of the heat conduction:

$$
S_D = \sum_{i \in N} \nabla \cdot (\rho (D_{eff} - \alpha_{eff}) c_{p,i} T (\nabla Y_i)). \qquad (2)
$$

The effective dynamic viscosity $\mu_{eff}$ is the sum of the molecular and turbulent or subgrid-scale viscosity regarding URANS and LES, respectively. $h$ is the sum of the internal energy per unit mass $e$ and the kinematic pressure $h = e + \frac{p}{\rho}$. According to the gradient flux approach, the thermal diffusivity results from $\alpha_{eff} = \frac{\mu}{\rho \cdot Pr} + \frac{\nu_{t/sgs}}{Pr_t}$ with the turbulent Prandtl number $Pr_t = 0.85$. The effective molecular diffusivity results from $D_{eff} = D + \frac{\nu_{t/sgs}}{Sc_t}$ with the turbulent Schmidt number $Sc_t = 0.85$. The molecular diffusivity $D$ is assumed to be constant. In the case of DNS the effective quantities reduce to their molecular counterpart. Mixture properties $\Phi_m$ are computed from the individual species properties $\Phi_i$ and species mass fractions $Y_i$ : $\Phi_m = \sum_{i \in N} Y_i \Phi_i$.

### *2.1.2. Case Definition*

The investigations are conducted using the DHC with aspect ratio 4, which is filled with air and 40 vol% of helium in the upper third, as shown in a schematic

sketch in Figure 1. Two different configurations of the DHC are considered. The reference case in Figure 1a is used for the calculation of result quantities, which are determined according to Equation 34 in Section 3.2. The reference case is defined with uniform temperature specification at the left and right wall, adiabatic walls at the top and bottom and with a helium layer, which is uniformly distributed in the upper third. The parameter variation case in Figure 1b serves for the actual study of uncertainties. For this configuration uncertain parameters are considered and will be further discussed in this section. The extensions of the computational domain are height $H$, width $W$, and depth $D$. The height-to-width aspect ratio and the width-to-depth aspect ratio are $\varphi_{HW} = H/W = 4$ and $\varphi_{WD} = W/D = 1$, respectively. The Prandtl numbers $Pr = 0.71$ and $Pr = 0.66$ used correspond to air and helium, respectively. The material values of air are used to define the Rayleigh number $Ra = \frac{g\beta\Delta T H^3 \rho}{\mu\alpha} = 2 \times 10^9$. The non-slip boundary condition is imposed on the velocity at the four enclosing walls. The cavity is subject to a temperature difference $\Delta T = \overline{T}_l - \overline{T}_r$. Thermal radiation is neglected. In case of URANS, 2D simulations are considered, while for DNS and LES, the third spatial dimension is taken into account due to the three-dimensional character of turbulent flow. Hence, the flow field is assumed to be periodic in the $z$-direction for LES and DNS. For the mass fraction, a zero-gradient at the enclosing walls is defined: $(\nabla Y \cdot \mathbf{n})|_{\partial\Omega} = 0$, where $\mathbf{n}$ denotes the wall-normal unit vector. For LES, a zero gradient is defined for the sub-grid scale viscosity and thermal diffusivity: $(\nabla \nu_{sgs} \cdot \mathbf{n})|_{\partial\Omega} = 0$, $(\nabla \alpha_{sgs} \cdot \mathbf{n})|_{\partial\Omega} = 0$. The Wall-Adapting Local Eddy-viscosity (WALE) model with $C_w = 0.5$ is applied to modelling viscous subgrid-scale effects [30]. For URANS, continuous wall functions are used for the eddy frequency, turbulent viscosity and thermal diffusivity, while a zero gradient boundary condition is defined for the turbulent kinetic energy. The wall treatment runs in low-Re formulation with $y^+ < 4$. The k-omega Shear Stress Transport (SST) turbulence model [31] is used with included buoyancy terms, based on the simple gradient diffusion hypothesis [32]. As initial conditions, temperature $T_0 = \overline{T} = 298.15\,\mathrm{K}$ and pressure $p_0 = 1\,\mathrm{bar}$ are applied. The material values for air and helium

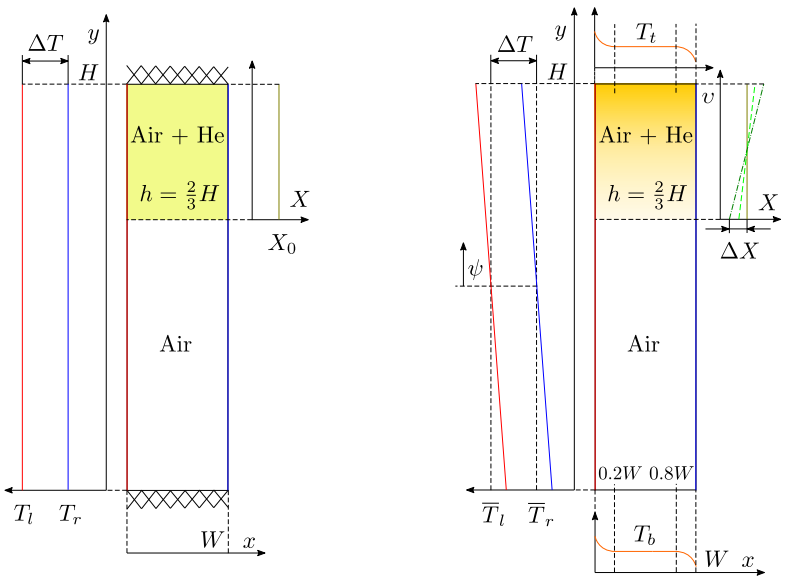


Figure 1: Schematic sketch of the Differentially Heated Cavity with illustration of uncertain parameters, such as the wall temperature difference, the wall-tangential temperature gradient, the top and bottom wall temperature and the initial helium stratification.

at $\overline{T} = 298.15\,\mathrm{K}$ and $p = 1\,\mathrm{bar}$ listed in Table 1 are applied. From this, the molecular diffusion coefficient, which was assumed to be constant, was also derived using Fuller's method [33] with $D_0 = 6.904 \times 10^{-5}\,\mathrm{m^2/s}$. The remaining properties are derived by the ideal gas law at $\overline{T} = 298.15\,\mathrm{K}$.

Table 1: Applied material properties of air and helium.

| Gas | Mole Weight $M$ | Isobaric Heat Capacity $C_p$ | Dynamic Viscosity $\mu$ | Prandtl Number $Pr$ |
|---|---|---|---|---|
| air [33] | $28.96\,\mathrm{g\,mol^{-1}}$ | $1006.5\,\mathrm{J\,K^{-1}}$ | $1.845 \times 10^{-5}\,\mathrm{Pa\,s}$ | 0.707 |
| helium [34] | $4.0\,\mathrm{g\,mol^{-1}}$ | $5193\,\mathrm{J\,K^{-1}}$ | $1.985 \times 10^{-5}\,\mathrm{Pa\,s}$ | 0.664 |

To investigate the propagation of uncertainties in the initial and boundary conditions as well as in material properties, input uncertainties were imposed through the definition of mutually independent random input variables. The uncertainties were chosen to be representative of possible uncertainties in the

THAI-TH32 experiment [10]. An illustration of the uncertain parameters is provided in Figure 1b. The uncertainties in the thermal boundary conditions include the wall temperature difference between the left and right walls, the vertical wall-tangential temperature gradient at the left and right walls, and the temperatures at the top and bottom walls of the cavity. Uncertainty in the initial helium stratification is modeled by a varying linear profile for the mole fraction $X$. The molecular diffusion coefficient $D$ is also considered as an uncertain parameter. The wall temperature difference between left and right wall is defined by

$$\overline{T}_{l/r} = \overline{T} \pm \frac{\Delta T}{2}, \quad \Delta T = (\Delta T)_{rel}\ \Delta T_0\ , \tag{3}$$

where $\Delta T_0 = 21.431\,\mathrm{K}$ is the reference temperature difference to obtain $Ra\ =\ 2 \times 10^9$, $(\Delta T)_{rel}$ describes the relative proportion of the reference temperature difference, and $\Delta T$ describes the actual temperature difference under consideration. The average temperature of the boundary is kept constant. The wall-tangential temperature gradient is defined with $\psi = y - H/2$ by the expression

$$T|_{l/r}\,(\psi) = \left(T_y|_{l,r}\right)_{rel} \frac{\Delta T}{H}\psi + \overline{T}_{l/r}\ , \tag{4}$$

where $\left(T_y|_{l,r}\right)_{rel}$ indicates the relative proportion of the temperature change due to the temperature gradient over the entire height to the characteristic temperature difference $\Delta T$. The bottom and top wall temperature is specified by the expression

$$T_{b/t} = \overline{T}_{r/l} \pm \left(T|_{b,t}\right)_{rel} \Delta T\ , \tag{5}$$

where $\left(T|_{b,t}\right)_{rel}$ is the relative proportion of the characteristic temperature difference $\Delta T$. To maintain consistency in the temperature field, a parabolic profile towards the corners and edges is applied, see [29]. The initial helium stratification is changed by variation of the initial mole fraction difference with $\upsilon = y - 2H/3$ by

$$X\,(\upsilon) = (\Delta X)_{rel}\,\frac{2X_0}{H-h}\upsilon + X_0\,(1 - (\Delta X)_{rel})\ , \tag{6}$$

where $(\Delta X)_{rel}$ is the relative proportion of the constant mole fraction $X_0 = 0.40$ of the reference case. The molecular diffusion coefficient results from

$$D = (D)_{rel}\ D_0\,, \tag{7}$$

where $(D)_{rel}$ is the relative proportion of the reference molecular diffusivity $D_0 = 6.904 \times 10^{-5}\,\mathrm{m}^2/\mathrm{s}$. Finally, model distributions $\mathcal{I}_\mathcal{Q}$ for the uncertain input variables $\mathcal{Q}_i$ with corresponding realizations $q_i$ were defined and are listed in Table 2. $\mathcal{N}\left(\mu, \sigma^2\right)$ and $\mathcal{LN}\left(\mu, \sigma^2\right)$ denote a normal distribution and a log-normal distribution with actual expectation $\mu$ and variance $\sigma^2$. $\mathcal{TN}\left(\mu, \sigma^2, a, b\right)$ denotes a truncated normal distribution with $a$ and $b$ as the lower and upper bounds. Further information regarding the definition of uncertain parameters can be found in [29].

Table 2: Definition of mutually independent random input variables

| $q_i$ | $\mathcal{Q}_i \sim \mathcal{I}_\mathcal{Q}$ | $q_i$ | $\mathcal{Q}_i \sim \mathcal{I}_\mathcal{Q}$ |
|---|---|---|---|
| $(\Delta T)_{rel}$ | $(\Delta\mathcal{T})_{rel} \sim \mathcal{N}\left(1, 0.1^2\right)$ | $(T_y\vert_{l,r})_{rel}$ | $(\mathcal{T}_y\vert_{l,r})_{rel} \sim \mathcal{LN}\left(0.1, 0.1^2\right)$ |
| $(T\vert_{b,t})_{rel}$ | $(\mathcal{T}\vert_{b,t})_{rel} \sim \mathcal{LN}\left(0.2, 0.1^2\right)$ | $(\Delta X)_{rel}$ | $(\Delta\mathcal{X})_{rel} \sim \mathcal{TN}\left(0, 0.2^2, 0, 1\right)$ |
| $(D)_{rel}$ | $(\mathcal{D})_{rel} \sim \mathcal{N}\left(1, 0.1^2\right)$ | | |

*2.1.3. Framework and Discretization*

The open-source C++ toolbox `OpenFOAM v.2006` [35, 36] was utilized for solving the nonlinear set of governing equations in a finite-volume framework. The pressure–velocity coupling was addressed by using the PIMPLE algorithm. It is ensured that the normalized residuals of the pressure-velocity coupling fall below the value $10^{-4}$, while for the matrix solvers below $10^{-6}$. The convective momentum flux was evaluated by second-order linear upwind. The remaining convective fluxes and diffusive fluxes were evaluated by the limited linear scheme. The convective flux of the helium mass fraction was discretized by the limited linear scheme that is bounded between 0 and 1. Temporal advancement was achieved by blending of 10% Euler and 90% Crank–Nicolson scheme, which is a good compromise between accuracy and robustness. It has been ensured

that the CFL number is always below the value of 0.5. The spatial grid resolution has to be fine enough to resolve most of the turbulent fluctuations for LES and fully resolve turbulence for DNS. In [29] the applied mesh refinement strategy is explained in detail and hence not repeated here. To ensure appropriate resolution of the wall-boundary layer, the dimensionless horizontal and vertical wall normal positions of the wall adjacent cell centroids are defined at $x_{\perp}^{+} \leq 1$ and $y_{\perp}^{+} \leq 1$. The mesh is refined linearly starting from the central planes of the cavity in the direction of the walls with a constant factor. The maximum dimensionless wall tangential cell sizes are set with $\Delta x_{\parallel}^{+} \approx 30$ and $\Delta y_{\parallel}^{+} \approx 30$ for LES and with $\Delta x_{\parallel}^{+} \approx 10$ and $\Delta y_{\parallel}^{+} \approx 10$ for DNS. A sufficient length in the periodic direction $\varphi_{WD} = W/D = 1$ is applied to ensure that turbulence fluctuations are uncorrelated at a separation of one half-period [11]. The mesh in the periodic direction is uniformly distributed with $\Delta z^{+} \approx 20$ for LES and DNS. A detailed description of the underlying mesh with supplementary grid convergence study can be found in [29].

### *2.2. Uncertainty Quantification*

The construction of Polynomial Chaos Expansions is described in Section 2.2.1, the stochastic representation via Karhunen-Loève Expansions is reported in Section 2.2.2, Section 2.2.3 presents the multifidelity modeling approach and the introduced Random Field Composition is explained in Section 2.2.4. Principles for variance-based decomposition and error estimation are provided in Section 2.2.5 and Section 2.2.6, respectively.

#### *2.2.1. Polynomial Chaos Expansions*

Non-intrusive Polynomial Chaos Expansions (PCE) [37, 38] were applied because of the high convergence rate of the stochastic results with an increasing number of simulation runs. Therefore, accurate results can potentially be obtained even with a moderate number of calculations. The random input variables $\boldsymbol{\mathcal{Q}} : \Omega \rightarrow \boldsymbol{\Upsilon} \subset \mathbb{R}^n$ are functions that map events $\omega \in \Omega$ from the sample space $\Omega$ to realizations $\mathbf{q} \in \boldsymbol{\Upsilon}$. PCE is a spectral method in which random

response functions $\mathcal{R}(\omega) = R(\boldsymbol{\mathcal{Q}})$ are described by suitable multidimensional orthogonal polynomials $\Psi_j(\boldsymbol{\mathcal{Q}})$ with corresponding expansion coefficients $\alpha_p$. The truncated polynomial chaos expansion, which is denoted by the function $S$, with $P$ terms and a limited number of random variables $n$ results in expression (8) [39, 40]:

$$\mathcal{R}^P(\omega) = S[R(\boldsymbol{\mathcal{Q}})] = \sum_{p=1}^{P} \alpha_p \Psi_p(\mathcal{Q}_1, \mathcal{Q}_2, \ldots, \mathcal{Q}_n) = \sum_{p=1}^{P} \alpha_p \Psi_p(\boldsymbol{\mathcal{Q}}) \tag{8}$$

where $p$ is the term based index for the series elements. The orthogonal polynomials are generated numerically by using the Gramm–Schmidt [41] approach. This allows us to define arbitrary probability density functions (PDFs) for the input variables and eliminates the need to induce additional nonlinearity through variable transformations. The expansion coefficients $\alpha_p$ are estimated by using discrete projection, which uses numerical integration techniques to determine the coefficients by the expression

$$\alpha_p = \frac{1}{\gamma_p} \mathbb{E}[R(\boldsymbol{\mathcal{Q}}) \Psi_p(\boldsymbol{\mathcal{Q}})] = \frac{1}{\gamma_p} \sum_{i=1}^{N} w^{(i)} R\left(\mathbf{q}^{(i)}\right) \Psi_p\left(\mathbf{q}^{(i)}\right) , \tag{9}$$

where $\mathbb{E}[\cdot]$ denotes the expectation and $w^{(i)}$ denote the quadrature weights for the respective quadrature points $\mathbf{q}^{(i)}$. The inner product $\gamma_j = \langle \Psi_j, \Psi_j \rangle_\varrho$ can be computed analytically and is defined w.r.t. the joint input PDF $\varrho_{\boldsymbol{\mathcal{Q}}}(\mathbf{q}) = \prod_{i=1}^{n} \varrho_{\mathcal{Q}_i}(q_i)$. Multidimensional integration is conducted using the Smolyak sparse grid method [42]. The sparse grid quadrature rule is defined by

$$\mathcal{A}(m,n) = \sum_{m+1 \le |\mathbf{l}| \le m+n} (-1)^{m+n-|\mathbf{l}|} \begin{pmatrix} n-1 \\ m+n-|\mathbf{l}| \end{pmatrix} \cdot \left(\mathcal{U}_{l_1}^{(1)} \otimes \cdots \otimes \mathcal{U}_{l_n}^{(1)}\right), \tag{10}$$

where $\mathcal{U}_{l_i}^{(1)}$ denotes one-dimensional quadrature operators with the level $l_i \in \mathbb{N}_+$ and $\mathbf{l}$ denotes the multi-index $\mathbf{l} = (l_1, \ldots, l_n) \in \mathbb{N}_+^n$. The dimension independent maximum sparse grid level $m$ controls the number of function evaluations and the associated accuracy of the PCE. The same sparse grid level $m = 2$ was chosen for DNS, LES as well as URANS to ensure comparability. Gaussian quadrature rules on an isotropic sparse grid are applied. For each index set of $\mathbf{l}$, the linear grow rule $g_i = 2l_i - 1$ is utilized for the corresponding one-dimensional

Gaussian quadrature orders $g_i$. The Gauss points and weights are computed by the Golub–Welsch [43] tridiagonal eigensolution. For sparse grid level $m = 2$, univariate and bivariate effects in $R$ are modeled with orthogonal polynomials of highest-order $a = 4$, resulting from the PCE construction according to [44]. The open-source software `Dakota 6.10` [45] was used as framework for the determination of polynomial chaos expansions.

### *2.2.2. Karhunen-Loève Expansions*

In the present work, random fields or stochastic processes are represented using Karhunen-Loève Expansions [46, 47, 48]. The method itself is known under a variety of names in different fields. In the field of CFD it is more widely used under the name Proper Orthogonal Decomposition (POD). The method is based on the spectral expansion of the process or field covariance function. The random field discretization comprises a finite linear combination of orthogonal deterministic basis functions multiplied by uncorrelated random variables. Let $\mathcal{R}(\boldsymbol{x}, \omega)$ be a random field (RF), which is dependent on the deterministic field variable $\boldsymbol{x} \in \mathcal{X}$ and random event $\omega \in \Omega$, where $\mathcal{X}$ denotes the field domain and $\Omega$ is the sample space. The RF can be divided into mean $\mu_{\mathcal{R}}(\boldsymbol{x})$ and a centered field $\mathcal{R}_0(\boldsymbol{x}, \omega)$ in the following way:

$$\mathcal{R}(\boldsymbol{x}, \omega) = \mu_{\mathcal{R}}(\boldsymbol{x}) + \mathcal{R}_0(\boldsymbol{x}, \omega). \tag{11}$$

Subsequently, the centered field $\mathcal{R}_0(\boldsymbol{x}, \omega)$ can be approximated through the truncated KLE of the RF

$$\mathcal{R}_0^K(\boldsymbol{x}, \omega) = \sum_{k=1}^{K} \sqrt{\lambda_k} \varphi_k(\boldsymbol{x}) \zeta_k(\omega), \tag{12}$$

where $\zeta_k(\omega)$ are mutually uncorrelated random variables with zero mean and unit variance. The scalars $\lambda_k$ and field-dependent deterministic functions $\varphi_k(\boldsymbol{x})$ are respectively the eigenvalues and orthogonal eigenfunctions to the homogeneous Fredholm equation of second kind:

$$\int_{\mathcal{X}} C(\boldsymbol{x}_a, \boldsymbol{x}_b) \varphi_k(\boldsymbol{x}_b) \, \mathrm{d}\boldsymbol{x}_b = \lambda_k \varphi_k(\boldsymbol{x}_a), \tag{13}$$

where

$$C\left(\boldsymbol{x}_a, \boldsymbol{x}_b\right) = \mathbb{E}\left[\mathcal{R}_0\left(\boldsymbol{x}_a, \omega\right) \mathcal{R}_0\left(\boldsymbol{x}_b, \omega\right)\right] \tag{14}$$

denotes the covariance function of $\mathcal{R}_0\left(\boldsymbol{x}, \omega\right)$. Furthermore, the orthonormality relation applies for the eigenfunctions:

$$\int_{\mathcal{X}} \varphi_k\left(\boldsymbol{x}\right) \varphi_l\left(\boldsymbol{x}\right) \mathrm{d}\boldsymbol{x} = \delta_{kl} \, . \tag{15}$$

The finite representation of RF by means of KLEs leads to minimization of the mean-square error and allows for efficient representation of the covariance kernel. All conducted calculations are based on spectral projection for the evaluation using PCEs and, therefore, expectation values for the random field $\mathcal{R}\left(\boldsymbol{x}, \omega\right)$ were determined with the same underlying numerical integration technique:

$$\mu_{\mathcal{R}}\left(\boldsymbol{x}\right) = \mathbb{E}\left[\mathcal{R}_0\left(\boldsymbol{x}, \omega\right)\right] = \sum_{i=1}^{N} w^{(i)} \, R\left(\boldsymbol{x}, \mathbf{q}^{(i)}\right) \, . \tag{16}$$

The covariance matrix $C_{ab}$ was constructed by taking the sample covariance

$$C_{ab} = \frac{1}{N-1} \sum_{i=1}^{N} R_0\left(x_a, \mathbf{q}^{(i)}\right) R_0\left(x_b, \mathbf{q}^{(i)}\right) \, , \tag{17}$$

because the square of the centered response functions yields complicated functions, that are difficult to approximate. The determination by means of the underlying quadrature for spectral projection led to larger errors compared to the estimation with the sample covariance. Random field data is stored at discrete field locations $\{x_j\}_{j=1}^{B}$. Thus, $x_a$ and $x_b$ represent discrete field location pairs. For solving the integral within the Fredholm equation, the discrete Karhunen-Loève method [49] is applied. Quadrature weights $w_b > 0$ are introduced, which reflect the local field width, e.g. for uniform discretization $w_b = \mathrm{X}/B$ is assigned, where X denotes the total field width. Consequently, the discretized and matrix form of Eq. 13 with the notations $C_{ab} = C\left(x_a, x_b\right)$ and $\varphi_{k,b} = \varphi_k\left(x_b\right)$ writes

$$\sum_{b=1}^{B} w_b \, C_{ab} \, \varphi_{k,b} = \lambda_k \, \varphi_{k,a} \;\; \Leftrightarrow \left(\mathbf{C}\mathbf{W}\right) \mathbf{\Phi} = \mathbf{\Phi}\mathbf{\Lambda} \, , \tag{18}$$

where $\mathbf{C} \in \mathbb{R}^{(B\times B)}$, $\mathbf{W} \in \mathbb{R}^{(B\times B)}$ is the diagonal quadrature weight matrix with $W_{bb} = w_b$. $\mathbf{\Phi}$ and $\mathbf{\Lambda}$ are the right eigenvector and eigenvalue matrix, respectively. Following [27, 28], the truncation of the KLE was accomplished through a practical rule based on the eigenvalue decay rate, i.e. terms with eigenvalues $\lambda_k$, which decayed to some fraction (e.g. 10%) of the largest eigenvalue $\lambda_1$, are omitted. In the present work, the decay rate $\lambda_{K+1}/\lambda_1 \leq 0.02$ was applied. According to [28, 27, 50], the mutually uncorrelated random variables $\zeta_k$ with zero mean and unit variance were approximated with PCE, to establish the relationship between $\mathcal{Q}_i$ and $\zeta_k$. This enables the combination of different KLEs in a multifidelity manner, which will be discussed in Section 2.2.3 in more detail. From the available simulation run data, for each mode $k$ corresponding values for $\zeta_k\left(\mathbf{q}^{(i)}\right)$ are derived through

$$\begin{aligned} \zeta_k(\omega) &= \frac{1}{\sqrt{\lambda_k}} \int_{\mathcal{X}} \mathcal{R}_0(\boldsymbol{x},\omega)\,\varphi_k(\boldsymbol{x})\,\mathrm{d}\boldsymbol{x} \\ \Rightarrow \zeta_k^{(i)} &= \frac{1}{\sqrt{\lambda_k}} \sum_{b=1}^{B} w_b\, R_0\left(x_b, \mathbf{q}^{(i)}\right)\, \varphi_k(x_b)\,. \end{aligned} \tag{19}$$

Subsequently, PCEs of the $\zeta_k$ random variables were created with the same coefficient determination procedure as described in Section 2.2.1 :

$$\zeta_k^P(\omega) = \sum_{p=1}^{P} \beta_{k,p} \Psi_p(\boldsymbol{\mathcal{Q}})\ . \tag{20}$$

In summary, the KLE combined with PCE can be described with the following expression by means of the PCE-basis and field-dependent expansion coefficients:

$$\mathcal{R}_0^{P,K}(\boldsymbol{x},\omega) = \sum_{p=1}^{P}\left[\sum_{k=1}^{K}\sqrt{\lambda_k}\varphi_k(\boldsymbol{x})\,\beta_{k,p}\right]\Psi_p(\boldsymbol{\mathcal{Q}}) = \sum_{p=1}^{P}\left[\alpha_p^K(\boldsymbol{x})\right]\Psi_p(\boldsymbol{\mathcal{Q}}) \tag{21}$$

### *2.2.3. Multifidelity Modeling*

The Multifidelity approach utilizes low-fidelity model predictions in addition to a reduced number of high-fidelity evaluations for building a MF–PCE. If the low-fidelity model (e.g. URANS) is able to capture useful trends of the high-fidelity model (e.g. LES), accurate UQ estimates can be achieved with

reduced computational effort with respect to single high-fidelity models [51]. Multifidelity PCE were first proposed by Ng and Eldred [52, 53]. Further improvement of the existing method was proposed by Berchier [54], which includes the correction by the high-fidelity evaluations based on the current polynomial chaos model. In the present work, the improved version is considered. The additive correction approach is explained in more detail below and reformulated with a recurrence relation in Equations 22. In the following, field-dependent random quantities or random fields are used within the notations for generalization.

As first step for the construction of MF models, a low-fidelity PCE model $\tilde{R}_1(\boldsymbol{x}, \boldsymbol{\mathcal{Q}}) = S_1[R_1(\boldsymbol{x}, \boldsymbol{\mathcal{Q}})]$ is computed, where $S_i$ denotes the truncated PCE approximation for the $i$th multifidelity level. Afterwards, a discrepancy function $D_{i+1}(\boldsymbol{x}, \boldsymbol{\mathcal{Q}})$ between the existing PCE model $\tilde{R}_1(\boldsymbol{x}, \boldsymbol{\mathcal{Q}})$ and a higher-fidelity computational model $R_{i+1}(\boldsymbol{x}, \boldsymbol{\mathcal{Q}})$ is computed and again approximated by PCE. The discrepancy PCE model $\tilde{D}_{i+1}(\boldsymbol{x}, \boldsymbol{\mathcal{Q}})$ is then added to the previous lower-fidelity model $\tilde{R}_i(\boldsymbol{x}, \boldsymbol{\mathcal{Q}})$ and yields the new model $\tilde{R}_{i+1}(\boldsymbol{x}, \boldsymbol{\mathcal{Q}})$, which can be improved by another even higher-fidelity model. For this purpose a discrepancy function is calculated again and finally added to the existing model. The approach can be extended to any number of fidelity-level $n+1$ and can thus be described with a recurrence relation as follows

$$\begin{aligned}
&\tilde{R}_1(\boldsymbol{x}, \boldsymbol{\mathcal{Q}}) = S_1[R_1(\boldsymbol{x}, \boldsymbol{\mathcal{Q}})], \qquad i = 1, \ldots, n \\
&D_{i+1}(\boldsymbol{x}, \boldsymbol{\mathcal{Q}}) = R_{i+1}(\boldsymbol{x}, \boldsymbol{\mathcal{Q}}) - \tilde{R}_i(\boldsymbol{x}, \boldsymbol{\mathcal{Q}}) \ , \\
&R_{i+1}(\boldsymbol{x}, \boldsymbol{\mathcal{Q}}) \approx \tilde{R}_{i+1}(\boldsymbol{x}, \boldsymbol{\mathcal{Q}}) = \tilde{D}_{i+1}(\boldsymbol{x}, \boldsymbol{\mathcal{Q}}) + \tilde{R}_i(\boldsymbol{x}, \boldsymbol{\mathcal{Q}}) .
\end{aligned} \tag{22}$$

In this way, PCEs and KLEs were derived from simulation runs according to sparse grid levels $m_i = (2, 1, 0)$ for URANS, LES and DNS, respectively, and combined to a MF model based on additive correction. The resulting MF model aims to approximate the high-fidelity DNS in a computationally efficient manner. This modeling approach was chosen as one example. In practice, any models with different model fidelity can be combined with each other, for example URANS with stepwise finer resolution (this is particularly referred to as multilevel) or with different physical models can be used.

*2.2.4. Random Field Composition*

Transient processes in the field of CFD are often characterized by highly dynamic behavior. For this reason, their stochastic representation in presence of uncertainties might be impeded. Therefore, a new approach for the representation of time-dependent stochastic processes $R(t, \boldsymbol{\mathcal{Q}})$ is proposed and used for the uncertainty analysis of the buoyancy-induced mixing process. Since every mixing process starts with the inhomogeneous state and ends with the fully mixed homogeneous state, the chronological progress of desired responses can be described by the mixing state. Responses can consequently be represented as a function of the mixing state and thereby the complexity of the response function can be reduced, if the considered mixing processes behave phenomenologically similar with respect to the mixing state. The mixing state is characterized by a suitable quantity $z$. Thus, if the response is approximated as a function of $z$, this yields the state-dependent random response field $Y(z, \boldsymbol{\mathcal{Q}})$. To establish the connection of the mixing state with physical time, the mixing state $z$ is also represented as a random field depending on time with $Z(t, \boldsymbol{\mathcal{Q}})$. Subsequently, realizations from the stochastic models $y^{(s)}$ and $z^{(s)}$ are derived from identical input parameters for the state-dependent response and for the time-dependent mixing state, respectively. As shown in the schematic representation in Equations 23, the functions $Y$ and $Z$ can be combined through function composition $Y(Z(t, \boldsymbol{\mathcal{Q}}), \boldsymbol{\mathcal{Q}})$ to provide a time-dependent model for stochastic

$$
\begin{array}{cc}
y = R|_{t=Z^{-1}} = R\left(Z^{-1}(z, \boldsymbol{\mathcal{Q}}), \boldsymbol{\mathcal{Q}}\right) = Y(z, \boldsymbol{\mathcal{Q}}) & z = Z(t, \boldsymbol{\mathcal{Q}}) \\
\Downarrow & \Downarrow \\
y^{(s)} = Y\left(z, \mathbf{q}^{(s)}\right) & z^{(s)} = Z\left(t, \mathbf{q}^{(s)}\right)
\end{array}
\tag{23}
$$

$$
\begin{array}{c}
r = R(t, \boldsymbol{\mathcal{Q}}) = Y|_{z=Z} = Y(Z(t, \boldsymbol{\mathcal{Q}}), \boldsymbol{\mathcal{Q}}) \\
\Downarrow \\
r^{(s)} = Y\left(Z\left(t, \mathbf{q}^{(s)}\right), \mathbf{q}^{(s)}\right)
\end{array}
$$

processes. This allows for the derivation of realizations of the time-dependent response $r^{(s)} = Y\left(Z\left(t, \mathbf{q}^{(s)}\right), \mathbf{q}^{(s)}\right)$ from related samples $y^{(s)}$ and $z^{(s)}$. Afterwards, the realizations $r^{(s)}$ can be statistically evaluated. Figure 2 shows a schematic sketch, which illustrates the RFC approach. At the top left one can see three field realizations for the state-dependent response $y^{(s)}$. At the bottom right, three field realizations for the time-dependent mixing state $z^{(s)}$ are shown. It becomes clear from the green highlighted realizations in Figure 2 that the response for each state and the corresponding elapsed time to reach that state is known. Consequently, the time-dependent response transients $r^{(s)}$, which are shown at the top right, can be derived. This derivation is illustrated using directional projection arrows between the plots in Figure 2. Starting from the plot for the state-dependent response at the top left, projection arrows, which are leading downward and projected on the corresponding realization for the

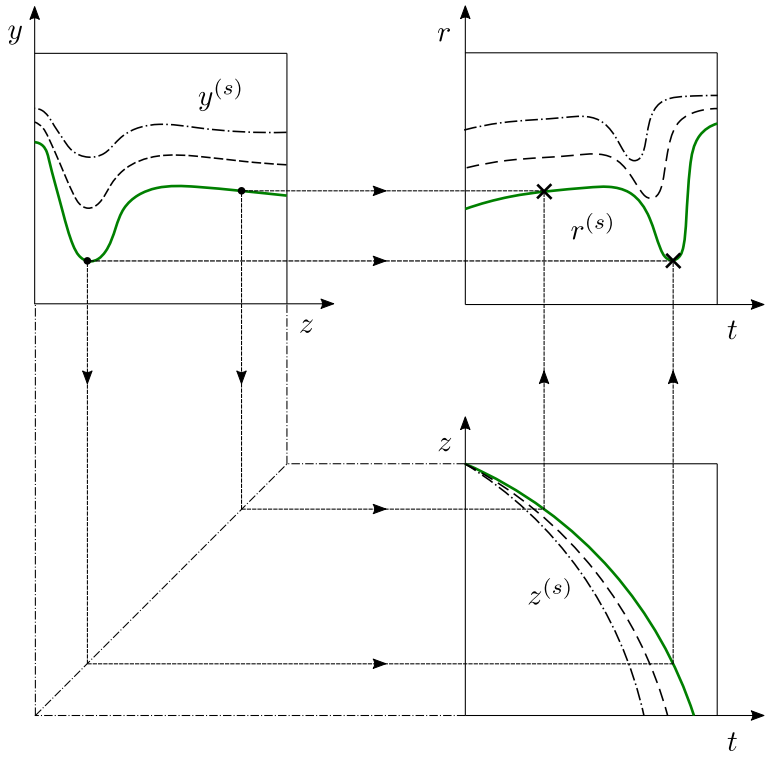


Figure 2: Schematic sketch of the Random Field Composition approach.

time-dependent state $z^{(s)}$, are used to determine the time that elapses for the respective state. Subsequently, the elapsed time to reach the respective state is projected upwards to the plot for the time-dependent response at the top right. Afterwards, the corresponding response value from the plot at the top left is projected to the plot at the top right. The intersection of the projection arrows from the response value and from the elapsed time gives a response point of the time-dependent response representation. The complete response function can thus be reconstructed from individual response points.

In this way, RFC allows for the description of the underlying stochastic processes $R(t, \boldsymbol{\mathcal{Q}})$ by means of less complex random fields $Y(z, \boldsymbol{\mathcal{Q}})$ and $Z(t, \boldsymbol{\mathcal{Q}})$, compared to straight consideration of the time-dependent stochastic process of the result quantities. This facilitates the approximation of stochastic processes with high accuracy even with a justifiable number of simulation runs.

### *2.2.5. Error Estimation*

According to [55], the accuracy of the truncated PCE models denoted by $\tilde{R}$ can be quantified by estimating the relative generalization error $\epsilon_{gen}$, which is defined as:

$$\epsilon_{gen} = \frac{\mathbb{E}\left[\left(R(\boldsymbol{\mathcal{Q}}) - \tilde{R}(\boldsymbol{\mathcal{Q}})\right)^2\right]}{\mathbb{V}\mathrm{ar}[\mathcal{R}]} \tag{24}$$

It is the expectation of the squared error normalized by the variance of the actual random response $\mathbb{V}\mathrm{ar}[\mathcal{R}]$. The estimation can be conducted using the expectation of the residual mean-square error by means of the quadrature rule, which is used for PCE coefficient calculation, and taking the variance of the PCE for normalization:

$$\epsilon_{res} = \frac{\sum_{i=1}^{N} w^{(i)} \left(R\left(\mathbf{q}^{(i)}\right) - \tilde{R}\left(\mathbf{q}^{(i)}\right)\right)^2}{\mathbb{V}\mathrm{ar}[\tilde{\mathcal{R}}]} \tag{25}$$

But the squared errors at hand are highly-nonlinear functions, which impede the calculation of expectation through numerical quadrature. Therefore, the

expectation of the squared error is determined using the estimator:

$$\tilde{\epsilon}_{res} = \frac{1}{N} \frac{\sum_{i=1}^{N} \left( R\left(\mathbf{q}^{(i)}\right) - \tilde{R}\left(\mathbf{q}^{(i)}\right) \right)^2}{\mathbb{V}\mathrm{ar}[\tilde{\mathcal{R}}]} \tag{26}$$

This allows the estimation of error relative to the local surrogate model variance. As global measure, the mean error estimate over the whole field or process domain $\mathcal{X}$ with the total field width X is determined as follows:

$$\langle \tilde{\epsilon}_{res} \rangle = \mathrm{X}^{-1} \int_{\mathcal{X}} \tilde{\epsilon}_{res}\left(\boldsymbol{x}\right) \mathrm{d}\boldsymbol{x} \; . \tag{27}$$

For the different stochastic models, the corresponding flow simulation realizations serve as a reference for the calculation of the error estimates. For the MF model, the DNS is used as a reference. The error is normalized by the variance of the stochastic model at hand.

### *2.2.6. Variance-Based Decomposition*

Uncertainties in responses can be apportioned to uncertainties in the input parameters through the determination of variance-based measures of sensitivity like the first-order Sobol indices $S_{\mathcal{Q}_i}$, the second-order Sobol indices $S_{\mathcal{Q}_i\mathcal{Q}_j}$ or the total-order Sobol indices $S_{T_{\mathcal{Q}_i}}$ [56]. Influence of univariate effects of individual input parameters can be quantified using $S_{\mathcal{Q}_i}$. Variance fractions, which are caused by interaction effects between input variables, can be determined by second-order Sobol indices $S_{\mathcal{Q}_i\mathcal{Q}_j}$ or higher-order indices. In the present work total-order indices $S_{T_{\mathcal{Q}_i}}$ are presented, which yield the full variance contribution of $\mathcal{Q}_i$ caused by its univariate impact and interactions of any order. It is given as

$$S_{T_i} = \frac{\mathbb{E}_{\boldsymbol{\mathcal{Q}}_{\sim i}}\left[\mathbb{V}\mathrm{ar}_{\mathcal{Q}_i}\left(\mathcal{R}|\boldsymbol{\mathcal{Q}}_{\sim i}\right)\right]}{\mathbb{V}\mathrm{ar}\left(\mathcal{R}\right)} = 1 - \frac{\mathbb{V}\mathrm{ar}_{\boldsymbol{\mathcal{Q}}_{\sim i}}\left[\mathbb{E}_{\mathcal{Q}_i}\left(\mathcal{R}|\boldsymbol{\mathcal{Q}}_{\sim i}\right)\right]}{\mathbb{V}\mathrm{ar}\left(\mathcal{R}\right)} \; , \tag{28}$$

where $\boldsymbol{\mathcal{Q}}_{\sim i}$ indicates the set of all random input variables except $\mathcal{Q}_i$. The sum of the total Sobol indices is always greater than or equal to one and thus it holds: $\sum_{i=1}^{n} S_{T_i} \geq 1$. This is due to the fact, that interaction effects are counted in both $S_{T_i}$ and $S_{T_j}$. The sum is equal to one or approximately one, if the response model has additive behavior with low interactions between the variables.

The Sobol-indices can be directly derived from a PCE representation [57]. For the RFC models, a Monte Carlo estimator is used for the derivation of the total-order indices [58]:

$$S_{T_i} \approx \frac{N-1}{2N} \frac{\sum_{j=1}^{N} \left( R\left(\mathbf{A}_j\right) - R\left( \left[\mathbf{A}_{\mathbf{B}}^{i}\right]_j \right) \right)^2}{\sum_{j=1}^{N} \left( R\left(\mathbf{A}_j\right) - \left[ N^{-1} \sum_{k=1}^{N} R\left(\mathbf{A}_k\right) \right] \right)^2}, \tag{29}$$

where $\mathbf{A}$ and $\mathbf{B}$ are two independent sample matrices. $\left[\mathbf{A}_{\mathbf{B}}^{i}\right]$ contains the elements for the $i$th input variable from the second matrix $\mathbf{B}$.

Variance-based decomposition allows for the complementary assessment of random fields and stochastic processes in Section 3.4 and 3.5 by enabling the assignment of response uncertainties to input uncertainties and by providing further insights into the physical behavior of stochastic processes at hand.

## 3. Results and Discussion

At first, the physical phenomenology of the mixing process within the DHC is explained in Section 3.1. Subsequently, the analyzed Quantities of Interest are introduced in Section 3.2, which is followed by results regarding Integral Quantities in Section 3.3. State-dependent Random Fields and time-dependent Stochastic Processes are presented and discussed in Section 3.4 and Section 3.5, respectively.

### *3.1. Physical Phenomenology*

In this section, the physical phenomenology of the mixing process within the DHC of the reference case is presented. This aims to facilitate the interpretation of the results. The mixing process comprises different consecutive phases, which are schematically shown over time in Figure 3. The mixing process is initialized with a quiescent stratification of helium and air, which is shown in a schematic sketch in Figure 3 on the left. The corresponding fluid property fields for the initial state are depicted in Figure 4. Due to the temperature difference between the left and right walls, a buoyancy-driven mixing process is initiated.

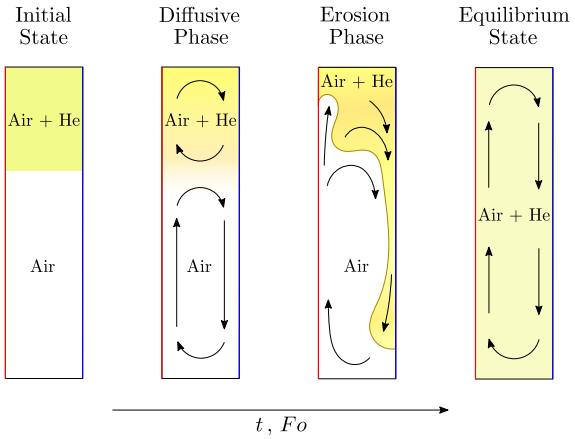


Figure 3: Schematic sketch for the consecutive phases of the mixing within the DHC.

Because of the different densities of the gas mixtures, two distinct circulating natural convection flows are established, one in the upper helium-rich region, and another in the lower air-rich region. During this stage, the mixing occurs mainly by diffusive mass transport. This diffusive phase is illustrated in Figure 3 and is also evident from the fluid property fields in Figure 5. The diffusive mixing persists until the density difference between the upper and lower region of the DHC is sufficiently small that the buoyancy forces become large enough to erode the remaining helium layer. This eventually leads to complete mixing

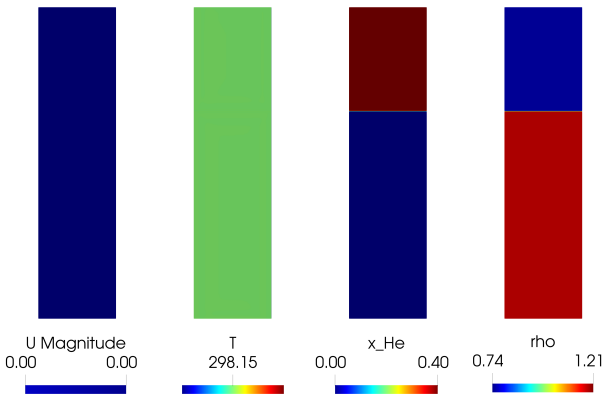


Figure 4: Fluid property fields from reference case DNS for the initial state at $Fo = 0$.

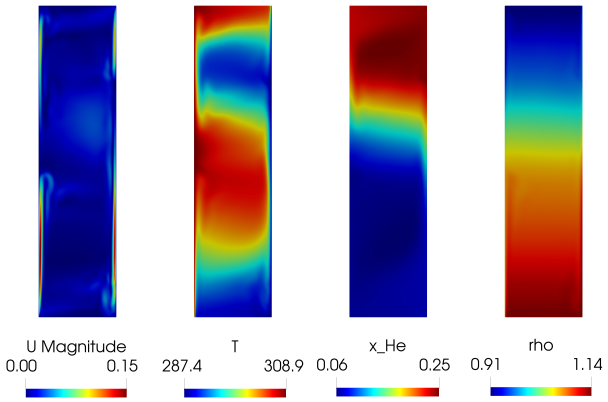


Figure 5: Fluid property fields from reference case DNS during the diffusive phase at $Fo = 3.1 \times 10^{-2}$.

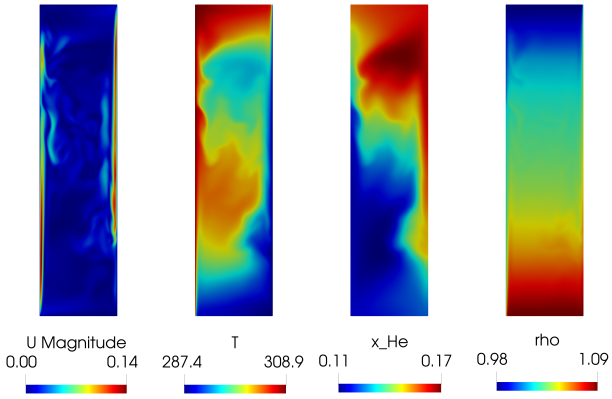


Figure 6: Fluid property fields from reference case DNS during the erosion phase at $Fo = 4.8 \times 10^{-2}$.

of air and helium. The erosion is schematically shown in Figure 3. The fluid property fields in Figure 5 also indicate this flow behavior. Dynamic transition stages, such as the erosion phase in particular, are characteristic for the prevailing physics inside the reactor test containment of the THAI test series. Thus, the testcase provides a good foundation for the subsequent application to the reactor test containment.

### 3.2. Quantities of Interest

For the uncertainty analysis of the buoyancy-driven mixing process, appropriate result quantities for further investigation are defined. These are referred to as Quantities of Interest (QoI) in the context of uncertainty quantification. Convective heat transfer is of great importance in natural convection flows. For this reason, the spatially averaged Nusselt number $Nu$ over the respective walls is analyzed, which provides information about the convective heat transfer in dimensionless form. It is determined by the expression

$$Nu = \frac{1}{A_{wall}} \int_{A_{wall}} \frac{\frac{\partial T}{\partial \mathbf{n}}\big|_{wall} H}{\Delta T} \mathrm{d}A \,, \tag{30}$$

where $\mathbf{n}$ denotes the wall-normal unit vector and $A_{wall}$ denotes the face area of the respective wall. The global kinetic energy is a measure of the occurring convection mechanisms. $E_k$ is the quotient of the global kinetic energy by a reference kinetic energy $\alpha^2 Ra/H^2$, which contains the material properties of air:

$$E_k = \left(\frac{\alpha^2}{H^2} Ra\right)^{-1} \cdot \frac{1}{M} \int_M \frac{1}{2} u^2 \mathrm{d}m \,. \tag{31}$$

$m$ denotes the mass and $M$ denotes the total mass in the fluid domain. Natural convection develops within the cavity and this leads to the gradual diffusive and convective mixing of the air and helium until the inhomogeneous mixture reaches the homogeneous state. The progress of the mixing process is quantified by the mixture uniformity $\sigma_X$, which is the volume-weighted standard deviation of the mole fraction $X$ from the homogeneous equilibrium state mole fraction $\bar{X}$ over the whole fluid domain. For normalization, the initial mixture uniformity $\sigma_{X_0}$ of the configuration with constant helium mole fraction $X_0 = 40\,\mathrm{vol\%}$ is used. This yields the following expression for the normalized mixture uniformity:

$$\Sigma_X = \frac{\sigma_X}{\sigma_{X_0}} = \frac{\sqrt{V^{-1} \int_V \left(X - \bar{X}\right)^2 \mathrm{d}V}}{\sqrt{V^{-1} \int_V \left(X_0 - \bar{X}\right)^2 \mathrm{d}V}} \,. \tag{32}$$

The mixing process starts from similar mixture uniformities depending on the initial stratification of the helium layer. Therefore, the initial inhomogeneous

state is characterized by $\Sigma_X \approx 1$. When the mixing proceeds, the normalized mixture uniformity finally takes on the value $\Sigma_X = 0$, which describes the homogeneous state. For this reason, a criterion for the quantification of the mixing time can be derived, and therefore, by definition of an upper bound $\Sigma_X \leq \epsilon_\Sigma = 10^{-3}$, which $\Sigma_X$ has to fall below, the achievement of the homogeneous state can be quantified. When considering mass transfer processes, the Fourier number $Fo = D_0\, t/H^2$ enables a dimensionless description of time. Hence, the time, when the homogeneous state is reached, can be described by $Fo_\epsilon = D_0\, t_\epsilon\, /H^2$.

Next to the temporal evolution of these result quantities, additional integral quantities, that describe the mixing process, were considered and facilitate the plain description of the transient profiles. For this purpose, the integral mean value $\langle R \rangle_{Fo_\epsilon}$ is formed over the respective mixing time in Eq. 33:

$$\langle R \rangle_{Fo_\epsilon} = Fo_\epsilon^{-1} \int_0^{Fo_\epsilon} R\,(Fo)\,\mathrm{d}Fo\,. \tag{33}$$

Moreover, the mean absolute deviation $\langle R' \rangle_{Fo_\epsilon}$ from the reference case, which was described in Section 2.1.2, over the reference mixing time $Fo_{\epsilon/ref}$ is defined in Eq. 34. For the different CFD models the corresponding flow simulation of the reference case serves as a reference.

$$\langle R' \rangle_{Fo_\epsilon} = Fo_{\epsilon/ref}^{-1} \int_0^{Fo_{\epsilon/ref}} |R\,(Fo) - R_{ref}\,(Fo)|\,\mathrm{d}Fo \tag{34}$$

Both integral quantities are illustrated with a schematic sketch in Figure 7. The reference case is freely selectable. In practice, the reference case could be selected in such a way that it corresponds to the simulation run with nominal values. The results for $\langle R' \rangle_{Fo_\epsilon}$ can then be used to assess the extent to which the reference results are affected on average when uncertainties are taken into account. By comparing the magnitudes of the deviations $\langle R' \rangle_{Fo_\epsilon}$ with those of the integral mean values $\langle R \rangle_{Fo_\epsilon}$, it is possible to determine whether the impact is significant or negligible.

From the integral quantities, complementary statements about the complete transient can be derived from a single scalar value. Subsequently, the temporal

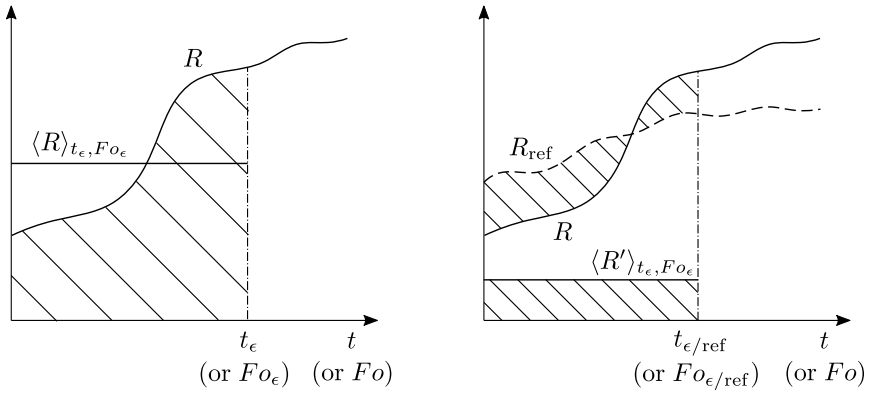


Figure 7: Schematic sketch for the interpretation of the integral quantities $\langle R \rangle_{Fo_\epsilon}$ and $\langle R' \rangle_{Fo_\epsilon}$.

evolution of quantities can be analyzed in more detail using the representation of stochastic processes and random fields.

### *3.3. Integral Quantities*

First of all, the integral quantities, which result from the buoyancy-driven mixing process, are presented and discussed. The integral mean and mean absolute deviation of QoI's, which include the Nusselt numbers $Nu$ at enclosing walls, the global kinetic energy $E_k$ and the normalized mixture uniformity $\Sigma_X$, are evaluated according to Section 3.2. Results regarding single-fidelity models like URANS, LES and DNS are shown in Figure 8, 9 and 10. The URANS-PCE, LES-PCE and MF-PCE fidelities are assessed in comparison to DNS-PCE with the respective probability density function, also written as $f_{\mathcal{R}}(R)$, resulting from the PCE surrogate. The PCE model accuracy itself is assessed through the determination of an error estimate $\tilde{\epsilon}_{res}$ based on the respective fidelity–model simulation runs, according to Section 2.2.5. In Figure 8a the PDFs for the mean Nusselt Number on the left wall $\langle Nu_l \rangle_{Fo_\epsilon}$ are depicted resulting from PCE surrogates. Compared to the DNS-results, LES slightly underestimates $\langle Nu_l \rangle_{Fo_\epsilon}$, whereas URANS slightly overestimates the mean Nusselt number on the left wall. The variance of URANS and LES agrees very well with the DNS, when comparing the dispersion of the different distributions. As a consequence

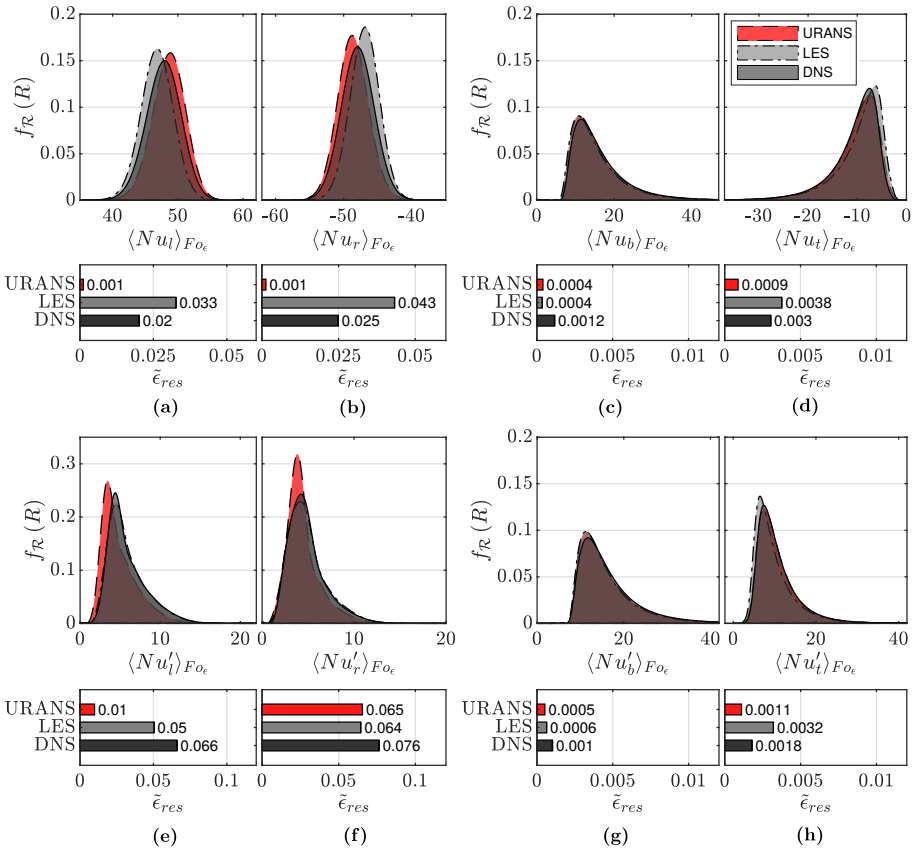


Figure 8: Single-fidelity PDFs and respective error estimates $\tilde{\epsilon}_{res}$ for Nusselt number: (**a,e**) on the left wall, $\langle Nu_l \rangle_{Fo_\epsilon}$ and $\langle Nu'_l \rangle_{Fo_\epsilon}$; (**b,f**) on the right wall, $\langle Nu_r \rangle_{Fo_\epsilon}$ and $\langle Nu'_r \rangle_{Fo_\epsilon}$; (**c,g**) on the bottom wall, $\langle Nu_b \rangle_{Fo_\epsilon}$ and $\langle Nu'_b \rangle_{Fo_\epsilon}$; and (**d,h**) on the top wall, $\langle Nu_t \rangle_{Fo_\epsilon}$ and $\langle Nu'_t \rangle_{Fo_\epsilon}$.

of the overestimation of the Nusselt number on the left wall by URANS, the Nusselt number on the right wall $\langle Nu_r \rangle_{Fo_\epsilon}$ in Figure 8b is underestimated, since larger incoming heat also causes more heat loss at the cold wall. The same applies for LES in a vice versa manner. Error estimates of up to $\tilde{\epsilon}_{res} \approx 0.04$,
370 which means the expectation of the squared error is 4% of the PCE variance, indicate, that the approximation of $Nu$ by means of PCE works very well. As depicted in Figures 8c-d, the PDFs for the top and bottom wall Nusselt number $\langle Nu_t \rangle_{Fo_\epsilon}$ and $\langle Nu_b \rangle_{Fo_\epsilon}$ nearly coincide with the DNS reference. The error that

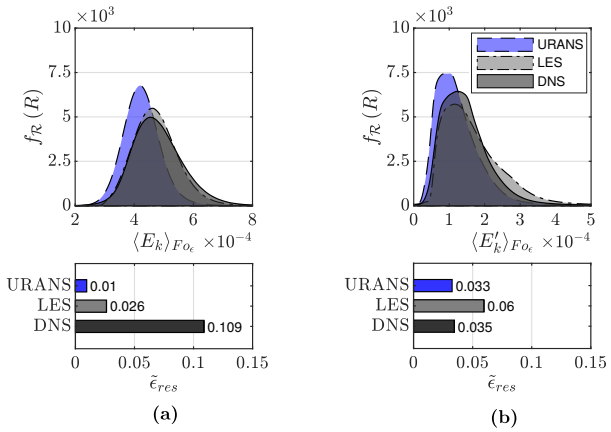


Figure 9: Single-fidelity PDFs and respective error estimates $\tilde{\epsilon}_{res}$ for global kinetic energy: (**a**) for $\langle E_k \rangle_{Fo_\epsilon}$; and (**b**) for $\langle E'_k \rangle_{Fo_\epsilon}$.

occurs due to the PCE approximation is negligible. The mean absolute deviation for the Nusselt numbers at the left and right wall $\langle Nu'_l \rangle_{Fo_\epsilon}$ and $\langle Nu'_r \rangle_{Fo_\epsilon}$ in Figures 8e,f shows that URANS predicts slightly lower variability compared to the well comparable LES and DNS. The error is still reasonably low. The PDFs for $\langle Nu'_t \rangle_{Fo_\epsilon}$ and $\langle Nu'_b \rangle_{Fo_\epsilon}$ in Figure 8g,h agree very well with small error estimates. The results for the global kinetic energy $\langle E_k \rangle_{Fo_\epsilon}$ and $\langle E'_k \rangle_{Fo_\epsilon}$ are depicted in Figure 9. LES is able to properly predict $\langle E_k \rangle_{Fo_\epsilon}$ in comparison with DNS. URANS underestimates the mean global kinetic energy with lower variance. According to the error estimates, the approximation of higher-fidelity models like DNS is impeded, because of increasing complexity in terms of spatial and temporal sensitivity of results with increasing fidelity level. For the prediction of $\langle E'_k \rangle_{Fo_\epsilon}$ deviations arise for both URANS and LES. Error estimates of the single PCE models are reasonably low.

The consideration of the mixing time measured by $Fo_\epsilon$, shown in Figure 10a, yields that URANS predicts the PDF very well. If one compares the PDF profiles, LES achieves a variance comparable to that of DNS, but underestimates the expectation. The integral mean value for the normalized mixture uniformity $\langle \Sigma_X \rangle_{Fo_\epsilon}$ in Figure 10b indicates differences between URANS, LES and DNS.

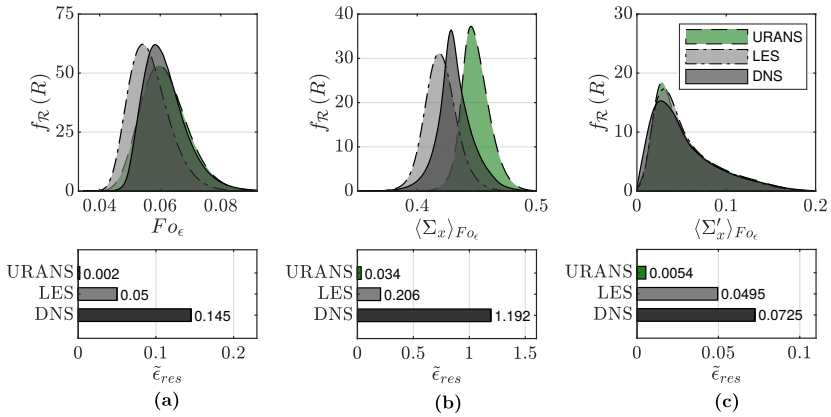


Figure 10: Single-fidelity PDFs and respective error estimates $\tilde{\epsilon}_{res}$ for mixing time and normalized mixture uniformity: (**a**) for $Fo_\epsilon$; (**b**) for $\langle\Sigma_X\rangle_{Fo_\epsilon}$; and (**c**) for $\langle\Sigma'_X\rangle_{Fo_\epsilon}$.

In this case, the error estimate yields a large error for the DNS–PCE, since the present PCE model mispredicted the expectation. For this reason, deviations of the DNS-PCE model from the simulation runs occur. The PDFs for $\langle\Sigma'_X\rangle_{Fo_\epsilon}$ in Figure 10c on the other hand show very good agreement between the DNS with LES and URANS. Consequently, the variability with respect to the reference case simulations is described very accurate through all single-fidelity models under investigation.

Table 3: Comparison of computational costs of single-fidelity and multifidelity PCE/KLE construction.

| Basis for the PCE/KLE construction | | Number of simulation runs | | | CPU time | | |
|---|---|---|---|---|---|---|---|
| | | URANS | LES | DNS | in core-h | rel. to DNS | rel. to LES |
| Single-fidelity | URANS | 105 | 0 | 0 | 1623 | 0.001 | 0.014 |
| | LES | 0 | 105 | 0 | 116559 | 0.08 | 1.0 |
| | DNS | 0 | 0 | 105 | 1451520 | 1.0 | 12.453 |
| Multifidelity | | 105 | 14 | 1 | 30988 | 0.021 | 0.266 |

Subsequently, results from multifidelity models are shown. Multifidelity Polynomial Chaos Expansions reduce the number of high-fidelity simulations and attain significant savings in computing resources while accurate results can be achieved simultaneously. As can be seen in Table 3, through the MF ap-

proach the computational cost for the determination of stochastic models was reduced to 2% compared to model construction based on single-fidelity DNS. Compared to the single-fidelity LES, the computational cost is merely 26.6%. PCE models for the QoI's were constructed from simulation runs according to sparse grid levels $m_i = (2, 1, 0)$ for URANS, LES and DNS, respectively, and combined in a multifidelity manner. The results are assessed by comparison with DNS-PCE and by determination of error estimates.

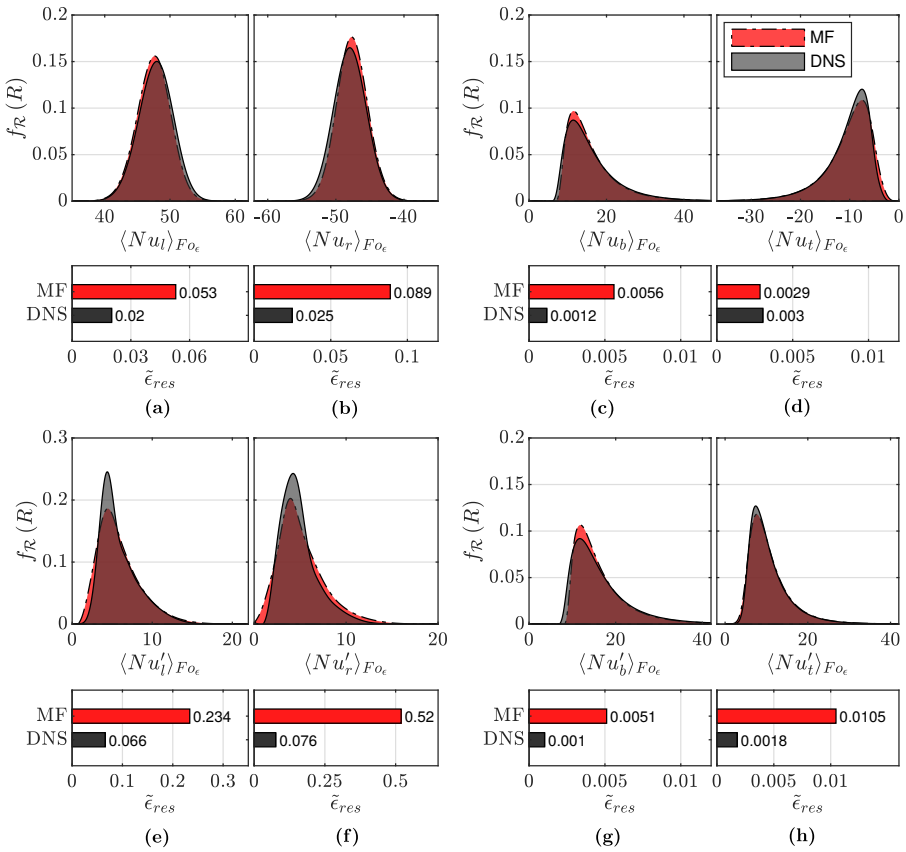


Figure 11: Multifidelity PDFs and respective error estimates $\tilde{\epsilon}_{res}$ for Nusselt number: (**a,e**) on the left wall, $\langle Nu_l \rangle_{Fo_\epsilon}$ and $\langle Nu_l' \rangle_{Fo_\epsilon}$; (**b,f**) on the right wall, $\langle Nu_r \rangle_{Fo_\epsilon}$ and $\langle Nu_r' \rangle_{Fo_\epsilon}$; (**c,g**) on the bottom wall, $\langle Nu_b \rangle_{Fo_\epsilon}$ and $\langle Nu_b' \rangle_{Fo_\epsilon}$; and (**d,h**) on the top wall, $\langle Nu_t \rangle_{Fo_\epsilon}$ and $\langle Nu_t' \rangle_{Fo_\epsilon}$.

Figures 11a-d demonstrate that the MF-PCE provides very accurate predictions of the integral mean Nusselt number at the enclosing walls. The distributions almost coincide and the occurring error, which is based on DNS runs, yields low values. Furthermore, the PDFs in Figure 11e-h show good agreement with the DNS distributions. However, the higher error estimates for $\langle Nu_l' \rangle_{Fo_\epsilon}$ and $\langle Nu_r' \rangle_{Fo_\epsilon}$ indicate that the model prediction deviates from the DNS in certain regions of the random input space.

The MF results for the integral mean global kinetic energy $\langle E_k \rangle_{Fo_\epsilon}$ in Figure 12a show that MF is able to predict a distribution with similar variance as for DNS but with a slightly shifted expectation. In addition, MF achieves a comparable error estimate like the DNS. For the prediction of $\langle E_k' \rangle_{Fo_\epsilon}$ in Figure 12b, on the other hand, a larger difference between the distribution for MF and DNS becomes clear. In this case, the lower-fidelity models in form of LES and URANS predict different trends than the DNS and the prerequisite for the MF approach is no longer completely fulfilled. This is due to the fact that the reference case, the calculation is based on, is different for URANS, LES and DNS. As a consequence, the error estimate $\tilde{\epsilon}_{res}$ returns larger values for MF. The results in Figure 13a regarding the mixing time $Fo_\epsilon$ show good agreement

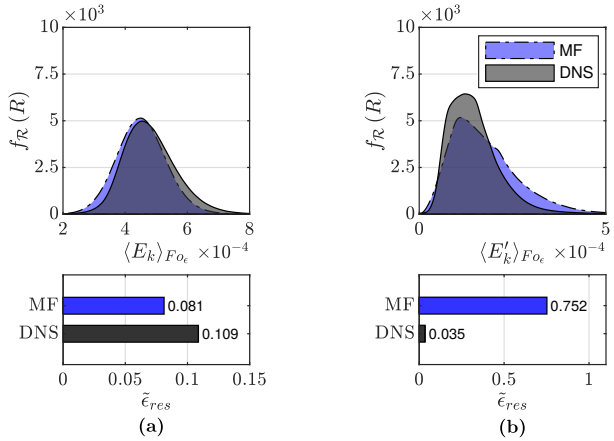


Figure 12: Multifidelity PDFs and respective error estimates $\tilde{\epsilon}_{res}$ for global kinetic energy: (**a**) for $\langle E_k \rangle_{Fo_\epsilon}$; and (**b**) for $\langle E_k' \rangle_{Fo_\epsilon}$.

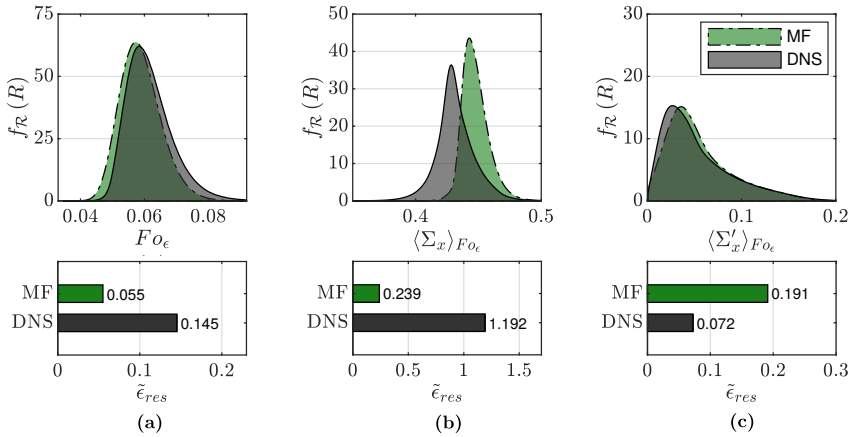


Figure 13: Multifidelity PDFs and respective error estimates $\tilde{\epsilon}_{res}$ for mixing time and normalized mixture uniformity: (**a**) for $Fo_\epsilon$; (**b**) for $\langle\Sigma_X\rangle_{Fo_\epsilon}$; and (**c**) for $\langle\Sigma'_X\rangle_{Fo_\epsilon}$.

with the DNS results and exhibit a lower error than the DNS surrogate model itself. This is due to the slightly incorrect estimation of the expectation for the DNS. The same situation occurs for the integral mean mixture uniformity $\langle\Sigma_X\rangle_{Fo_\epsilon}$. The MF model yields an error estimate, which is even lower than for DNS indicating faster convergence of the PCE in the former case. The PDFs for $\langle\Sigma'_X\rangle_{Fo_\epsilon}$ in Figure 13c on the other hand show very good agreement between the DNS and MF with an acceptable error.

The evaluation using scalar integral quantities provides a first insight for the assessment of stochastic processes or random fields. But for detailed investigation, the consideration of the chronological progress, instantaneous flow features and sensitivities is essential. Therefore, state-dependent random fields are derived in the following section and finally, representations for the underlying stochastic processes are constructed using the proposed Random Field Composition.

### *3.4. State-dependent Random Fields*

The construction of models for the representation of stochastic processes, which occur during the buoyancy-induced mixing process, is associated with difficulties, since the transient profiles show highly dynamic behavior. Thus,

the approximation of time-dependent stochastic processes by means of PCE or KLE with respect to time, leads to poor results, when it comes to dynamic effects, as will be shown in Section 3.5. A huge number of simulation runs would be required for the approximation of strong nonlinear effects within the transient with a stochastic model. For this reason, the RFC approach is used for the description of highly dynamic transient processes with justifiable computational effort. This includes the partitioning of the stochastic process into less complex random fields. The state variable was chosen to be the normalized mixture uniformity $z = \Sigma_X$, which describes the mixing state. Based on this, the representation of the stochastic process comprises the respective random responses $Y(\Sigma_X, \boldsymbol{\mathcal{Q}})$, such as heat flow, velocities or local concentrations, together with the random elapsing time through the Fourier number $Fo = \mathcal{F}o(\Sigma_X, \boldsymbol{\mathcal{Q}})$, each as a function of the normalized mixture uniformity $\Sigma_X$. Next to the benefits of using RFC, the representation of the random fields as a function of the mixing state through $\Sigma_X$ allowed for consistent construction of the MF model, because PCEs, which describe the same condition or mixing state, were compared and improved by the discrepancy function. In the following, the random fields $Nu_l(\Sigma_X, \boldsymbol{\mathcal{Q}})$, $E_k(\Sigma_X, \boldsymbol{\mathcal{Q}})$ and $\mathcal{F}o(\Sigma_X, \boldsymbol{\mathcal{Q}})$ are discussed for the investigation of heat transfer, convection mechanisms and mixing progress, respectively. The evaluations were conducted for the single-fidelity models URANS, LES and DNS along with MF models. Corresponding results are shown in Figure 14.

The RF were approximated with KLE in conjunction with PCE. The KLEs were truncated such that: $\lambda_{K+1}/\lambda_1 \leq 0.02$. Sample realizations $\zeta_k^{(i)}$ for each mode $k$ with respect to the simulation realizations were calculated. PCEs for $\zeta_k$ were built using the Smolyak sparse grid method. Consistency of the Karhunen-Loève theorem is fulfilled, since expectation values for $\zeta_k$ are close to zero, the variance is approximately one and $\zeta_k$ are mutually uncorrelated. Since the major interest of the investigation lies in the consideration of transient mean profiles, field realizations for KLE construction were filtered with a gaussian kernel with standard deviation $\sigma = 0.005 \cdot \mathrm{X}$, where X denotes the total field width of the domain. This also allows dynamic buoyancy oscillations and turbulent fluctua-

tions to be filtered out and facilitates approximations with numerical models.

Statistics for the characterization of the presented RF comprise the expectation $\mu$, the expectation plus and minus the standard deviation $\mu \pm \sigma$, the median $Q_{0.50}$ and quantiles $Q$. Regions between pairwise quantiles are highlighted with color. The quantile intervals of the random fields $Nu_l\left(\Sigma_X, \boldsymbol{\mathcal{Q}}\right)$, $E_k\left(\Sigma_X, \boldsymbol{\mathcal{Q}}\right)$ and $\mathcal{F}o\left(\Sigma_X, \boldsymbol{\mathcal{Q}}\right)$ are highlighted in red, blue and green, respectively. Quantile intervals $[Q_a, Q_b]$ towards median are shown progressively darker. From the statistics in Figure 14, it can be deduced that the mixing process consists of

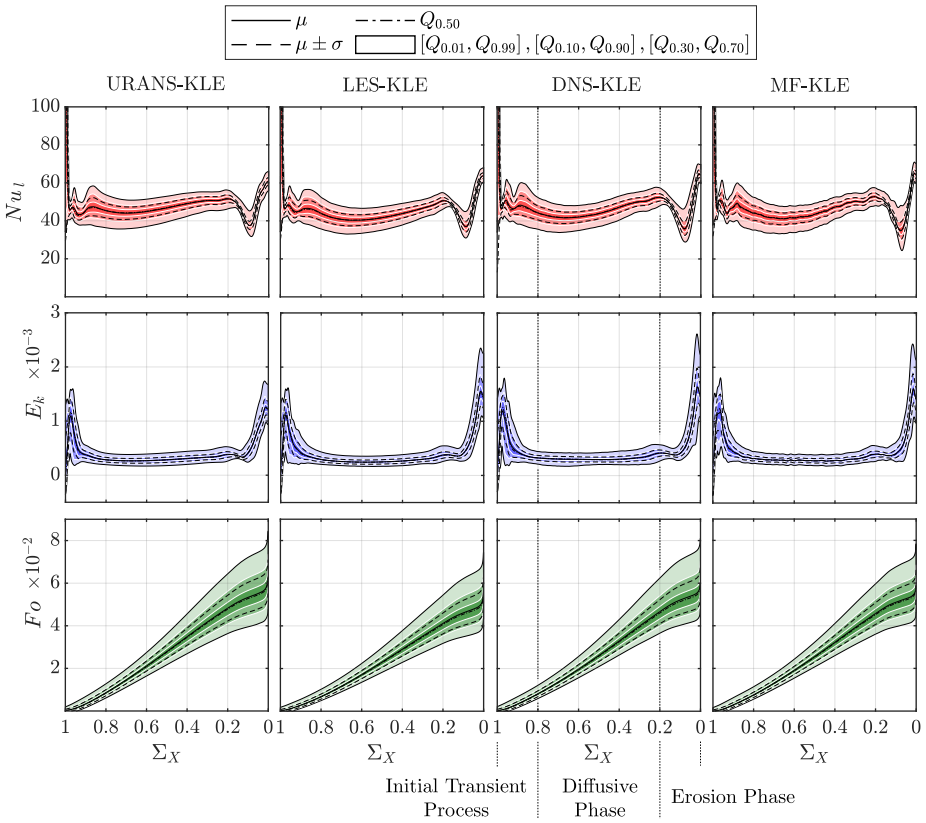


Figure 14: State-dependent random fields over normalized mixture uniformity $\Sigma_X$ shown column-wise for URANS, LES, DNS and MF and row-wise for the left-wall Nusselt number $Nu_l$, for the global kinetic energy $E_k$ and for time by the Fourier number $Fo$.

different phases. The profiles for $E_k$ reveal that the mixing process starts with an initial transient process, followed by a diffusive mixing phase with stagnant amount of kinetic energy and a final convective erosion phase, which is characterized by the steep increase in kinetic energy at the end. This is also evident from the profiles for the Nusselt number showing initially oscillating values, stagnant consecutive magnitudes for $Nu_l$ and a final undershoot, which takes place during erosion. Almost constant slope at the beginning and decreasing slope of the mean profile for $Fo$ also provide an indication for the described behavior.

If one takes a closer look at the individual RF's, Figure 14 shows that the URANS-KLE model slightly overestimates $Nu_l$ during the diffusive phase $\{\Sigma_X | 0.8 \geq \Sigma_X \geq 0.2\}$ compared to the DNS-KLE model. Moreover, the variance during erosion $\{\Sigma_X | 0.2 \geq \Sigma_X \geq 0\}$ is predicted with lower values than for the DNS-KLE. The LES-KLE, on the other hand, is able to capture the progress behavior, but also provides a slightly lower variance prediction in the interval $\{\Sigma_X | 0.4 \geq \Sigma_X \geq 0\}$ compared to the DNS-KLE. The MF–KLE yields good results regarding the profile and the variance. Minor oscillations can be seen in the visualization of the MF results. These originate from the correction with the second discrepancy function between LES-KLE and DNS-KLE, each of which includes a single simulation. Therefore, dynamic processes over time become visible. The profiles for $E_k$ show, that the URANS-KLE underestimates the global kinetic energy during the erosion $\{\Sigma_X | 0.1 \geq \Sigma_X \geq 0\}$, if the DNS-KLE is considered as a reference. Regarding the erosion, the LES-KLE provides comparable predictions to the DNS-KLE. The MF-KLE leads to further improvement of the prediction accuracy. In the initial transient process as well as in the diffusive phase, all models provide similar predictions.

The statistical results regarding $Fo$ for URANS-KLE match well with the DNS-KLE. In comparison, the URANS-KLE predicts a slightly larger uncertainty band. It is noticeable, that the LES-KLE underestimates the mixing time, as already discussed by means of $Fo_\epsilon$ in Section 3.3, and this leads to time-shifted statistics towards lower values. Nevertheless, the results for the

MF-KLE again show good agreement with DNS-KLE results. For $Fo\,(\omega)$, the URANS-KLE would provide an already sufficient accuracy level and building a surrogate based on multiple fidelities would not be necessary. In large-scale applications, however, the accuracy of the respective model with regard to a random response variable is unknown and a detailed assessment using reference results (e.g. in form of DNS) is infeasible. Therefore, when using the MF approach, the assumption is made that the incremental increase in model accuracy also increases the prediction accuracy. However, this does not have to be inevitably the case for the description of highly-nonlinear dynamic systems encountered in CFD.

As stated before, the final erosion process of the mixing process is characterized by its dynamic behavior and its strong time dependency. For this reason, the construction of stochastic representations is impeded. Therefore, RF are constructed over the mixture uniformity $\Sigma_X$, which facilitates stochastic mod-

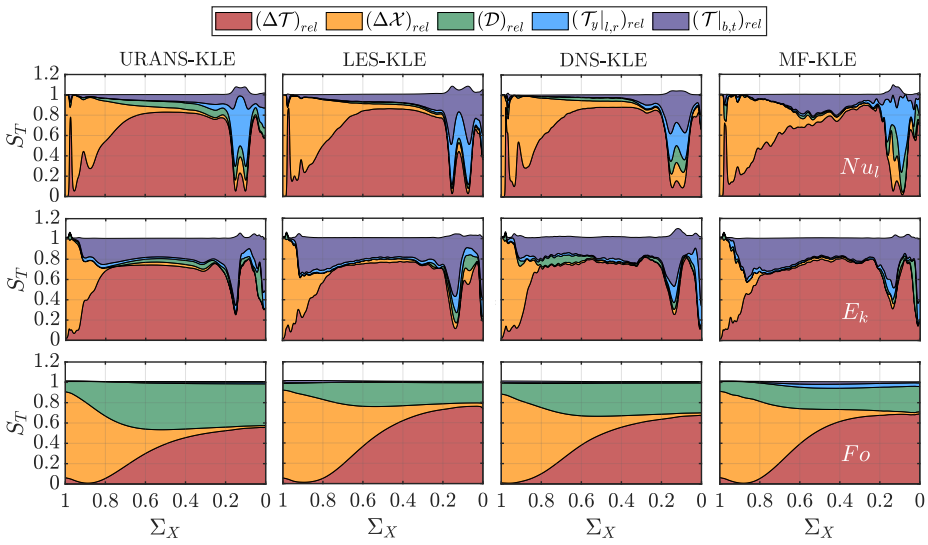


Figure 15: Stacked total-order Sobol Indices $S_{T_i}$ over normalized mixture uniformity $\Sigma_X$ shown column-wise for URANS, LES, DNS and MF and row-wise for the left-wall Nusselt number $Nu_l$, for the global kinetic energy $E_k$ and for time by the Fourier number $Fo$.

eling. As shown in Figure 15, the total-order Sobol indices reveal nearly additive character of the RFs, since they sum up approximately to one: $\sum_{i=1}^{n} S_{T_i} \approx 1$. Interaction effects are thus significantly reduced compared to the straight time-dependent consideration, which will be discussed in more detail in the next Section. As can be seen in Figure 15, the variance of all quantities at the beginning of the mixing process is mainly determined by the initial structure of the helium stratification, which changes due to the uncertain parameter $(\Delta\mathcal{X})_{rel}$. In terms of heat transfer measured by the left-wall Nusselt number $Nu_l$, the variance after the initial process is mainly caused by the uncertain characteristic temperature difference $(\Delta\mathcal{T})_{rel}$ and the uncertain temperatures of the bottom and top wall $(\mathcal{T}|_{b,t})_{rel}$. The same also applies for the global kinetic energy $E_k$. During the erosion, however, both $Nu_l$ and $E_k$ show a very complex variance behavior. The stacked total-order Sobol indices for the elapsed time in form of $Fo$ show that the variance is initially caused by the uncertain structure of the helium layer through $(\Delta\mathcal{X})_{rel}$. Subsequently, the mixing process mainly proceeds by the influence of the uncertain characteristic temperature difference $(\Delta\mathcal{T})_{rel}$ and the uncertain molecular diffusion coefficient $(\mathcal{D})_{rel}$.

In the next section, results for the description of time-dependent stochastic processes, which characterize the uncertain buoyancy-driven process, are discussed.

### *3.5. Time-dependent Stochastic Processes*

For transient processes, which are subject to uncertainties, it is of particular importance to approximate the temporal evolution of QoI's within the possible random space. The stochastic model has to be sufficiently accurate and reliable in order to draw conclusions. For the investigated buoyancy-driven mixing process, the construction of a precise stochastic model is not readily possible in practice. The straight representation of the underlying stochastic processes of QoI's in terms of time is impeded through the strong time-dependency of the convective erosion process, which takes place inside the cavity at the end of the mixing process. This physical behavior is also characteristic for the onset of

convective erosion during the buoyancy-driven mixing process inside the reactor test containment. After initial diffusive mixing, the erosion of the helium layer begins at a certain point in time. The dynamic effects, which occur during this erosion process, are difficult to approximate. Nevertheless, for the construction of reliable stochastic models and for the derivation of statistics, this transient behavior has to predicted in a proper way.

In the following, results for the representation of the time-dependent stochastic processes $Nu_l\,(Fo, \boldsymbol{\mathcal{Q}})$, $E_k\,(Fo, \boldsymbol{\mathcal{Q}})$ and $\Sigma_X\,(Fo, \boldsymbol{\mathcal{Q}})$ are discussed and analyzed in more detail. The stochastic processes are visualized with the expectation $\mu$, the expectation plus and minus the standard deviation $\mu \pm \sigma$, the median $Q_{0.50}$ and with quantiles $Q$. Regions between pairwise quantile functions are highlighted with color.

First of all, the single-fidelity statistics and error estimates, which were derived from the time-dependent KLE models based on DNS runs, are presented

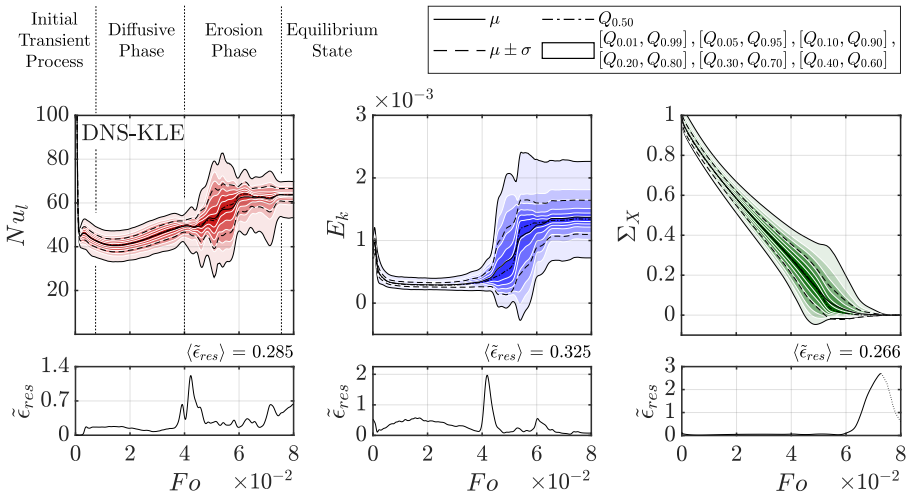


Figure 16: Statistics and error estimate $\tilde{\epsilon}_{res}$ derived from KLE model in terms of time for the time-dependent stochastic processes of DNS over time via dimensionless Fourier number $Fo$: (**a**) Left-wall Nusselt number $Nu_l$;
(**b**) global kinetic energy $E_k$; and (**c**) normalized mixture uniformity $\Sigma_X$.

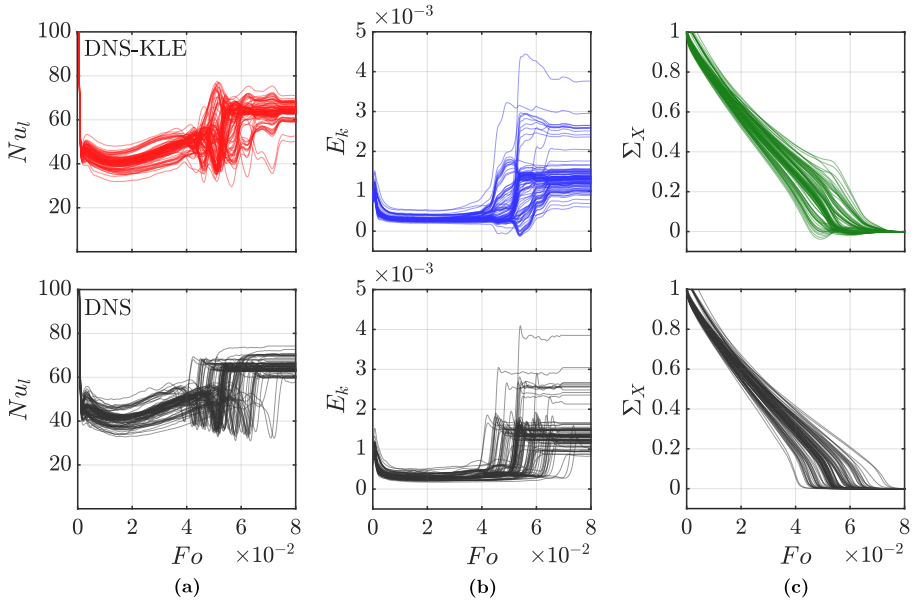


Figure 17: Temporal profile realizations from input parameters for stochastic model construction over time via dimensionless Fourier number $Fo$ shown row-wise for time-dependent KLE model and DNS runs: (**a**) Left-wall Nusselt number $Nu_l$; (**b**) the global kinetic energy $E_k$; and (**c**) normalized mixture uniformity $\Sigma_X$.

in Figure 16 to indicate the model deficiencies that occur, when stochastic models were built directly with respect to time. Furthermore, differences between temporal profiles of DNS runs and derived temporal profiles from constructed KLE models, which are shown in Figure 17, substantiate appearing inaccuracies of the model. From Figures 16a-c one can observe from the temporal evolution of the error estimate $\tilde{\epsilon}_{res}$, that the QoI's are reasonably predicted in the time interval $\{Fo|\, 0 \leq Fo \leq 0.04\}$. However, at the onset of dynamic processes due to convective erosion during the interval $\{Fo|\, 0.04 \leq Fo \leq 0.08\}$, deviations are indicated. This error is also manifested in the statistics, which especially becomes visible from the strongly oscillating profiles for $Nu_l$ and $E_k$ in Figure 16a-b. In Figure 17, temporal profiles for the derived KLE model, which result from the same input parameters as for the construction of the stochastic model, reveal that the model leads to mispredictions compared to corresponding

DNS results after the start of convective erosion. It can be assumed, that the actual error is larger than the error estimate indicates, since the error estimate is derived with the conducted simulation runs on the basis of which the KLE model was constructed and consequently works best. But, as the model does not fully represent the physics correctly, the error might be larger for other parameter input combinations.

Based on these findings, efforts were made to overcome this model deficiency. As shown in Section 3.4, the chronological progress of the mixing process can be described by the mixing state, with respect to which the mixing processes are phenomenologically similar i.e. timing of erosion takes place at comparable mixing states. The derivation of these state-dependent random fields allows for representation of stochastic processes through their combination via RFC. As shown in Equations 35, state-dependent random response fields $Y\left(\Sigma_X, \boldsymbol{\mathcal{Q}}\right)$ were considered together with the random field for elapsed time for the achievement of a mixing state $\mathcal{F}o\left(\Sigma_X, \boldsymbol{\mathcal{Q}}\right)$. By means of function composition, response realizations $r^{(s)}$ for the input parameters $\mathbf{q}^{(s)}$ with respect to the input PDFs were derived. Subsequently, statistics like estimates of the expectation $\mu$, standard deviation $\sigma$ or quantiles $Q$ were determined.

$$\begin{array}{cc} y = R|_{Fo=\mathcal{F}o} = R\left(\mathcal{F}o\left(\Sigma_X, \boldsymbol{\mathcal{Q}}\right), \boldsymbol{\mathcal{Q}}\right) & Fo = \mathcal{F}o\left(\Sigma_X, \boldsymbol{\mathcal{Q}}\right) \\ \Leftrightarrow y = Y\left(\Sigma_X, \boldsymbol{\mathcal{Q}}\right) & \Leftrightarrow \Sigma_X = \mathcal{F}o^{-1}\left(Fo, \boldsymbol{\mathcal{Q}}\right) \\ \Downarrow & \Downarrow \\ y^{(s)} = Y\left(\Sigma_X, \mathbf{q}^{(s)}\right) & \Sigma_X^{(s)} = \mathcal{F}o^{-1}\left(Fo, \mathbf{q}^{(s)}\right) \end{array} \tag{35}$$

$$\begin{array}{c} r = R\left(Fo, \boldsymbol{\mathcal{Q}}\right) = Y|_{\Sigma_X = \mathcal{F}o^{-1}} = Y\left(\mathcal{F}o^{-1}\left(Fo, \boldsymbol{\mathcal{Q}}\right), \boldsymbol{\mathcal{Q}}\right) \\ \Downarrow \\ r^{(s)} = Y\left(\mathcal{F}o^{-1}\left(Fo, \mathbf{q}^{(s)}\right), \mathbf{q}^{(s)}\right) \end{array}$$

Results, which were obtained from the RFC approach, are presented hereinafter. Single-fidelity statistics from URANS (Figure 18), LES (Figure 19), DNS (Figure 20) and from the additive MF model (Figure 21) are discussed. The results are presented in the same manner as before. Starting with the results from URANS (Figure 18) concerning the left-wall Nusselt number $Nu_l$ in Figure 18a, it becomes clear once again that URANS is slightly overestimating the Nusselt number in the early diffusive phase $\{Fo|\, 0 \leq Fo \leq 0.04\}$, when the results for DNS in Figure 20a are taken as reference. This has already been observed during the evaluation of the state-dependent fields in Section 3.4.

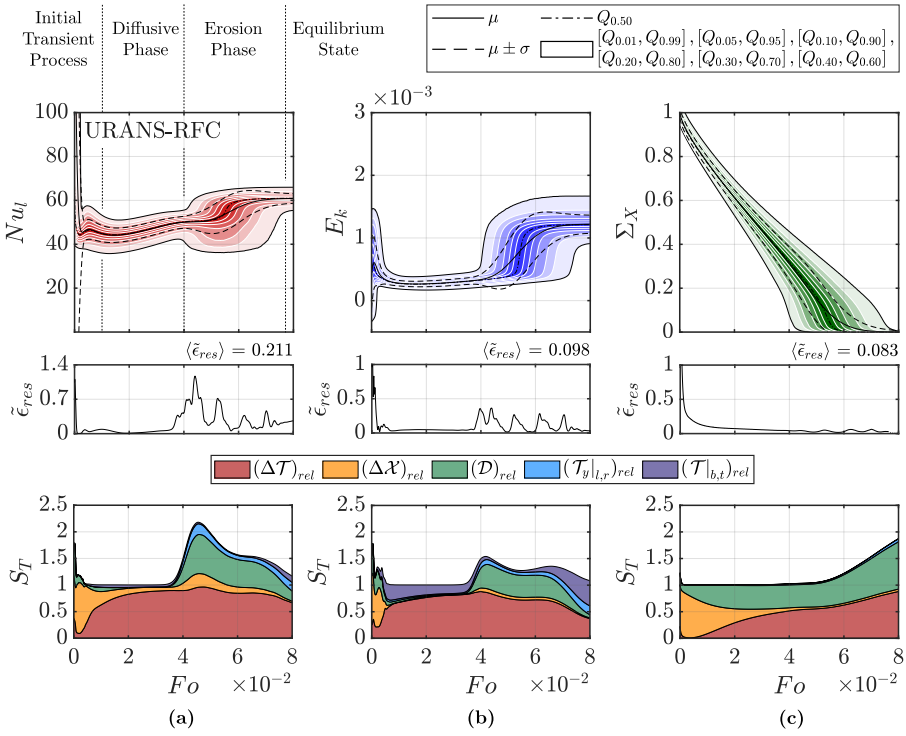


Figure 18: Statistics, error estimates $\tilde{\epsilon}_{res}$ and stacked total-order Sobol indices $S_T$ derived from RFC model in terms of state for the time-dependent stochastic processes of URANS over time via dimensionless Fourier number $Fo$:

(**a**) Left-wall Nusselt number $Nu_l$; (**b**) global kinetic energy $E_k$; and

(**c**) normalized mixture uniformity $\Sigma_X$.

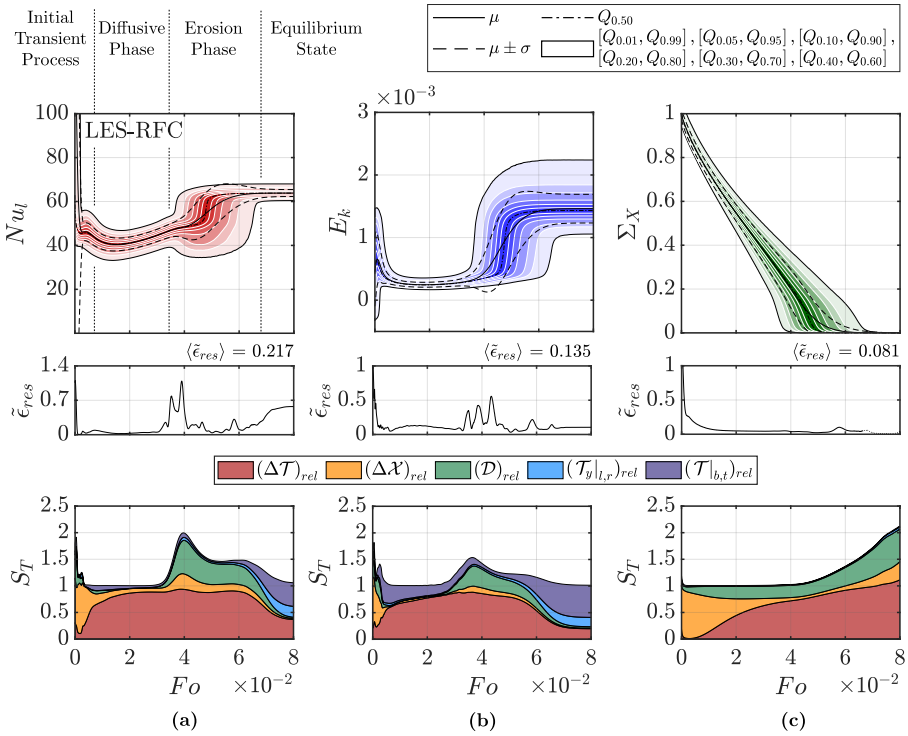


Figure 19: Statistics, error estimates $\tilde{\epsilon}_{res}$ and stacked total-order Sobol indices $S_T$ derived from RFC model in terms of state for the time-dependent stochastic processes of LES over time via dimensionless Fourier number $Fo$:
(**a**) Left-wall Nusselt number $Nu_l$; (**b**) global kinetic energy $E_k$; and
(**c**) normalized mixture uniformity $\Sigma_X$.

In addition, the results for the integral mean value for the Nusselt number $\langle Nu_l \rangle_{Fo_\epsilon}$ in Section 3.3 provided a first indication for the overestimation. As noted in the discussion of state-dependent fields, the uncertainty band is narrower during the erosion phase $\{Fo|\, 0.04 \leq Fo \leq 0.08\}$ compared to the DNS. The predictions based on LES (Figure 19) for $Nu_l$ in Figure 19a show correct temporal behavior with respect to profile shape and variance. However, the mixing time is underestimated by LES and as a result, the profiles are shifted to lower values in time. From Figure 21a it is noticeable, that MF is able to reflect the DNS results very well. Slight differences are visible for the quantiles

during the erosion phase.

Regarding the global kinetic energy $E_k$, one can state that URANS in Figure 18b predicts lower values during erosion than the DNS and thus a smaller uncertainty band, which is characterized by the quantiles. LES (Figure 19b) is able to predict the magnitude of the kinetic energy, but with shifted profiles in time. MF (Figure 21b), on the other hand, allows for proper prediction of $E_k$ in terms of magnitude and timing. The initial transient process and the diffusive phase is predicted in a similar manner by all single-fidelity and multifidelity models.

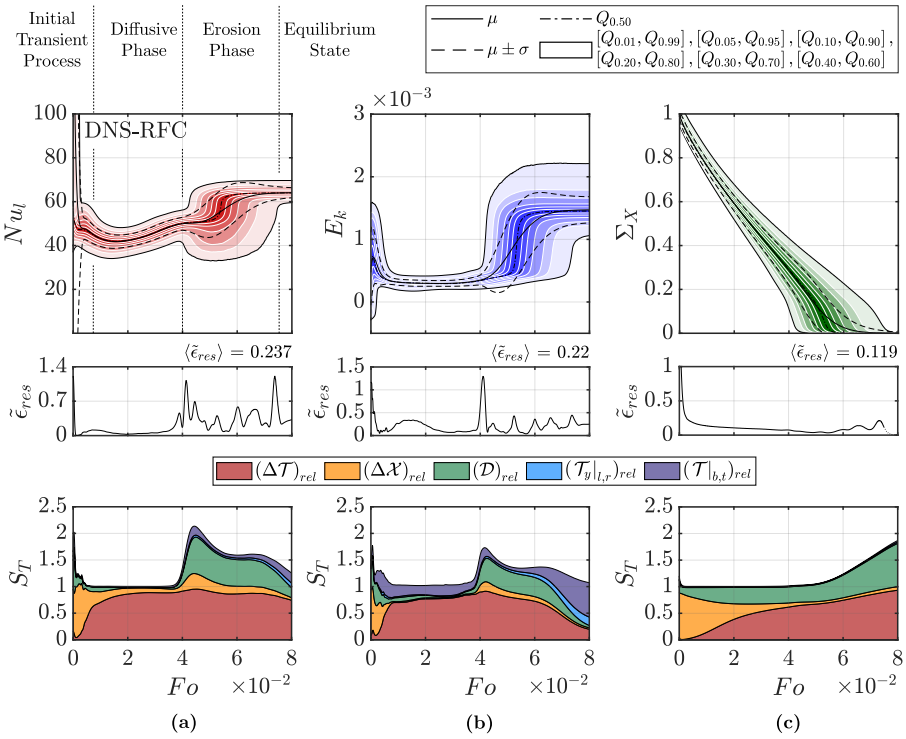


Figure 20: Statistics, error estimates $\tilde{\epsilon}_{res}$ and stacked total-order Sobol indices $S_T$ derived from RFC model in terms of state for the time-dependent stochastic processes of DNS over time via dimensionless Fourier number $Fo$:

(**a**) Left-wall Nusselt number $Nu_l$; (**b**) global kinetic energy $E_k$; and

(**c**) normalized mixture uniformity $\Sigma_X$.

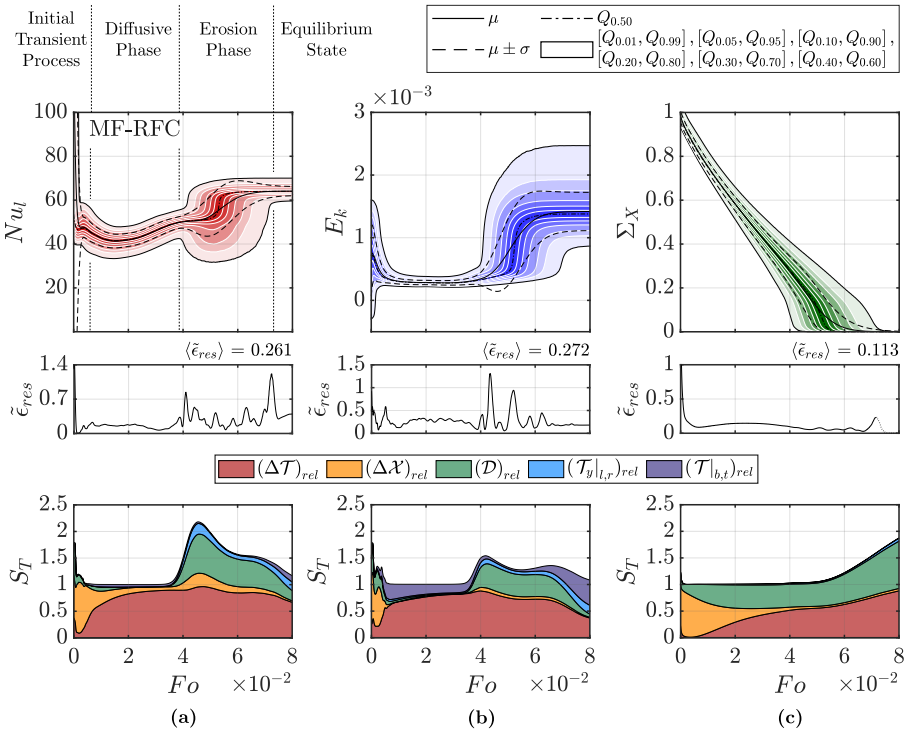


Figure 21: Statistics, error estimates $\tilde{\epsilon}_{res}$ and stacked total-order Sobol indices $S_T$ derived from RFC model in terms of state for the time-dependent stochastic processes of MF model over time via dimensionless Fourier number $Fo$:
(**a**) Left-wall Nusselt number $Nu_l$; (**b**) global kinetic energy $E_k$; and
(**c**) normalized mixture uniformity $\Sigma_X$.

The statistics for $\Sigma_X$ from URANS in Figure 18c show very good agreement with the DNS in Figure 20c. The dispersion is slightly overestimated. There is also good agreement between the LES in Figure 19c with DNS. However, by virtue of the underestimation of mixing time, the profiles are shifted in time. Finally, the multifidelity model (Figure 21c) also manages to accomplish comparable results to the DNS.

The temporal profile realizations from DNS runs and from RFC model derivation, which were drawn from input parameters for stochastic model construction, are depicted in Figure 22. RFC models, which are based on stochastic

KLE models from DNS and MF, achieve comparable physical behavior when compared with DNS runs in bottom Figure 22. There are merely mispredictions during the initial transient process. However, the diffusive mixing and highly dynamic erosion mechanisms, which are of major interest, are correctly reproduced by the stochastic models. Comparison of the DNS-RFC results in Figure 22 with the DNS-KLE results in Figure 17 clearly highlight the better performance of the RFC methodology compared to the straight KLE construction in terms of time.

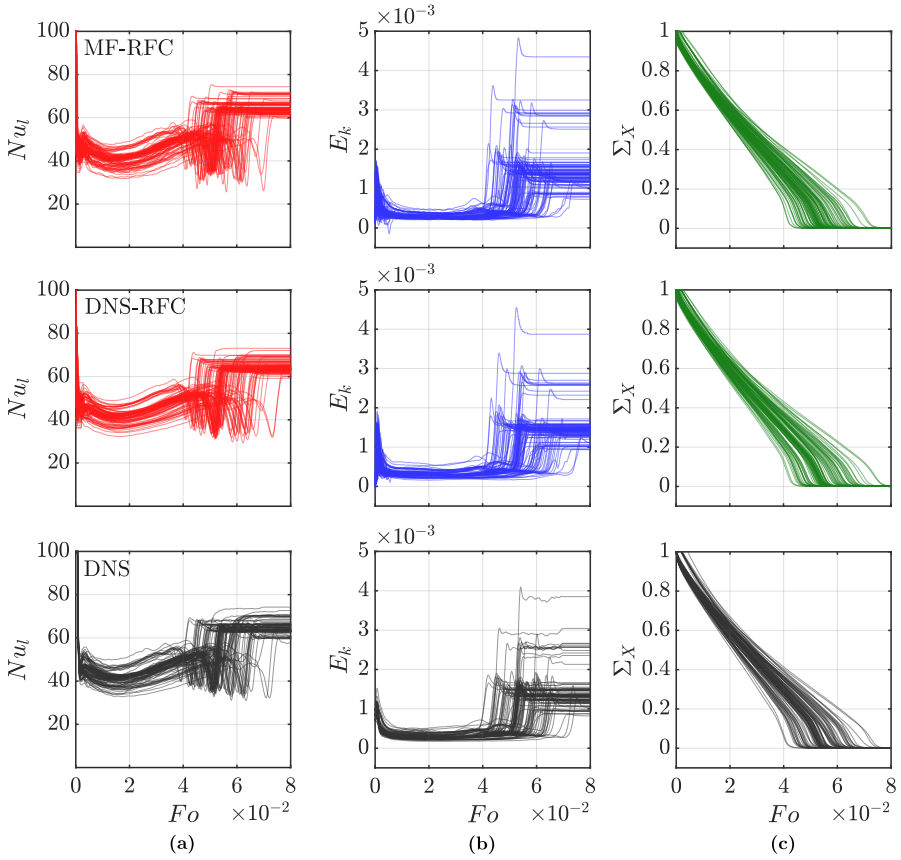


Figure 22: Temporal profile realizations from input parameters for stochastic model construction over time via dimensionless Fourier number $Fo$ shown row-wise for MF-RFC, DNS-RFC and DNS: (**a**) Left-wall Nusselt number $Nu_l$;
(**b**) the global kinetic energy $E_k$; and (**c**) normalized mixture uniformity $\Sigma_X$.

The stacked total-order Sobol indices in Figures 18 - 21, which are calculated based on RFC, also confirm the benefits of the RFC approach, if one compares the results with the state-dependent Sobol indices from Figure 15 in Section 3.4. During the diffusive phase, the time-dependent random responses exhibit additive behavior according to Figure 18 - 21. But the start of the erosion phase, on the other hand, is accompanied by strong interaction effects between the random input variables, since the sum of $S_{T_i}$ clearly exceeds the value of one. Consequently, the approximation of interaction effects is facilitated by partitioning the stochastic process into individual random fields within RFC. It becomes clear, that at the beginning of the mixing process the variance of all random responses is mostly caused by the initial structure of the helium stratification, which changes due to the uncertain parameter $(\Delta\mathcal{X})_{rel}$. The variance of mixing state measured by $\Sigma_X$ is mainly based on the uncertain characteristic temperature difference $(\Delta\mathcal{T})_{rel}$ and the uncertain molecular diffusion coefficient $(\mathcal{D})_{rel}$, as can be seen in Figures 18 - 21c. The uncertain characteristic temperature difference $(\Delta\mathcal{T})_{rel}$ also shows major influence on $Nu_l$ and $E_k$ in Figures 18 - 21a,b. Since transient effects, such as the convective erosion process, depend on the mixing progress and thus on time, the uncertain input parameter $(\mathcal{D})_{rel}$, which significantly contributes to the progress of the mixing process next to $(\Delta\mathcal{T})_{rel}$, leads to considerable proportion of the variance for $Nu_l$ and $E_k$ after the start of the erosion.

Finally, complementary error estimates $\tilde{\epsilon}_{res}$ for the presented RFC models are discussed. As can be seen in Figures 18 - 21, the temporal evolution of the estimates $\tilde{\epsilon}_{res}$ also show that the error takes on larger values at the beginning of the mixing process. This is due to the fact, that the initial transient processes within the possible random space proceed similar in terms of time and therefore, in turn approximation is hindered by the state-dependent perspective. Hence, the time-dependent KLE model in Figure 17 provides good predictions for the initial transient process at the beginning, but less precise results when state-dependent dynamic processes occur.

Furthermore, when looking at the error estimates $\tilde{\epsilon}_{res}$ in Figures 18-21, error

peaks are still evident during the erosion phase for $Nu_l$ and $E_k$, due to the model prediction of erosion time, which deviates from the reference simulation runs. But after the stochastic model transient catches up the simulation transient, the error decreases again. For the determination of the mean error estimate $\langle\tilde{\epsilon}_{res}\rangle$ of $\Sigma_X$ values until the expectation reaches zero are considered, since the variance subsequently becomes negligibly small. In summary, the results for the mean error estimate $\langle\tilde{\epsilon}_{res}\rangle$ show that $\Sigma_X$ is well predicted, whereas for $Nu_l$ and $E_k$, it indicates potential model improvement through additional simulation runs and further model refinement. As an engineering approach, the model deficiencies for the initial transient process could be eliminated by considering the individual phases separately i.e. the initial transient process is investigated as a time-dependent stochastic process, because the phenomena occur synchronously, whereas the diffusive and erosion phase is analyzed with state-dependent random fields and RFC. Through the division into individual field or time domains, single random field or stochastic process representations can be determined with the locally advantageous properties, and thus the overall prediction accuracy can be increased.

## 4. Conclusions

Predictions of complex phenomena by means of computational models are often subject to uncertainties. Computational Fluid Dynamics of thermal hydraulics within light water reactor containments is one representative for numerical models, which is associated with uncertainties, whose consideration is of great importance. As a basis for the uncertainty analysis of buoyancy-driven mixing processes within the THAI test vessel, methodologies for the assessment of uncertainties were established using a generic test case, which corresponds to the Differentially Heated Cavity. An initial stratification with 40 vol% helium next to air was defined in the upper third. Due to the formation of natural convection, a buoyancy-driven mixing process takes place in the enclosure. Arising uncertainties in Quantities of Interest, which originate from uncertain

input parameters, were evaluated using stochastic spectral methods, such as Polynomial Chaos Expansions and Karhunen-Loève Expansions. The stochastic representations in this paper include results for scalar random responses, random fields as well as stochastic processes. Single-fidelity CFD models like Unsteady Reynolds-Averaged Navier–Stokes, Large Eddy Simulation, and Direct Numerical Simulation are analyzed and combined to three–level multifidelity models. The investigation of total-order Sobol indices allowed for the assignment of variance proportions to the individual random input variables and further insights into stochastic response behavior were gained. Error estimates were determined for the assessment of the respective model accuracy. In addition, Random Field Composition is introduced, as a promising approach for the description of highly-dynamic stochastic processes.

First, uncertain integral result quantities were approximated by PCEs. The stochastic models for these quantities facilitated the plain description of transient profiles and allowed for a first derivation of statements about occurring heat transfer, convection and mixing behavior. Differences between the individual single-fidelity approaches became apparent. As a solution, MF models were deduced, which attained comparable results to the DNS and allowed for a significant reduction up to 98% of the computing time in comparison to model construction based on single-fidelity DNS.

Subsequently, the aim was to approximate time-dependent stochastic processes at hand. For this purpose, Random Field Composition was introduced and applied. To this end, the stochastic processes were partitioned into single random fields for the QoI's as a function of the mixing state through the construction of KLEs. Stochastic models for single-fidelity and multifidelity random fields were derived in this way. The representation of state-dependent random fields for the result quantities leaded to less complex approximations in comparison to the time-dependent stochastic processes, since the mixing process remains phenomenologically similar with changing parameters regarding the input uncertainties. Afterwards, function composition of the individual random fields allowed for the coupled representation of the stochastic processes. The

derived statistics revealed that URANS or LES slightly deviate from results regarding DNS. The present MF models accomplish good agreement with the DNS reference. Hence, MF models have potential for the achievement of higher accuracy compared to single lower-fidelity models at moderate extra cost.

In industrial practice, uncertainty analysis of high-fidelity models, like DNS, is uneconomical or not even feasible with the available resources. Hence, for the accomplishment of reliable results for uncertainties in complex large-scale applications and to ensure the feasibility of computations with justifiable effort, multifidelity models, which can be built from any different model types as by using different mesh resolution or different modeling approaches, provide a good basis and making assumptions serves as a reasonable trade-off between accuracy and required computational resources. In addition, RFC achieved efficient stochastic representation of highly-dynamic transient processes, which also characterize the unsteady flow behavior within the THAI-TH32 experiment. As a practical lesson, the following can be inferred for future studies. The fundamental concept behind RFC involves the simplification of functions, that need to be approximated, by identifying patterns or relationships within the underlying phenomenon, which is investigated. If the function to be approximated can be decomposed into less complex components, this can lead to a reduction in the number of computational runs, which are required to approximate the overall function. As a result, the model construction process is computationally efficient from the outset. Therefore, the promising RFC approach together with multifidelity modeling serves as an appropriate methodology for uncertainty quantification of large-scale applications and will be pursued in further investigations of the application-oriented THAI-TH32 CFD validation case.

## Acknowledgments

Parts of the work presented in this paper are funded by the German Federal Ministry for the Environment, Nature Conservation, Nuclear Safety and Consumer Protection (BMUV, grant No. 1501595) on the basis of a decision

by the German Bundestag. The computational resources for this project have been provided by the Gauss Centre for Supercomputing/Leibniz Supercomputing Centre under the project name pn29ce.

## References

[1] B. L. Smith, M. Andreani, U. Bieder, F. Ducros, E. Graffard, M. Heitsch, M. Henriksson, T. Höhne, M. Houkema, E. Komen, J. Mahaffy, F. Menter, F. Moretti, T. Morii, P. Mühlbauer, U. Rohde, M. Scheuerer, C.-H. Song, T. Watanabe, G. Zigh, Assessment of CFD Codes for Nuclear Reactor Safety Problems, Tech. Rep. January, OECD/NEA/CSNI (2014).

[2] Z. Liang, M. Sonnenkalb, A. Bentaib, M. Sangiorgi, Status Report on Hydrogen Management and Related Computer Codes, Tech. rep., OECD/NEA/CSNI (2014).

[3] OECD / SETH-2 Project PANDA and MISTRA Experiments Final Summary Report - Investigation of Key Issues for the Simulation of Thermal- hydraulic Conditions in Water Reactor Containment, Tech. rep., OECD/NEA/CSNI (2012).

[4] S. Gupta, E. Schmidt, B. Von Laufenberg, M. Freitag, G. Poss, F. Funke, G. Weber, Thai test facility for experimental research on hydrogen and fission product behaviour in light water reactor containments, Nuclear Engineering and Design 294 (2015) 183–201. doi:10.1016/j.nucengdes.2015.09.013.

[5] S. Kelm, J. Lehmkuhl, W. Jahn, H. J. Allelein, A comparative assessment of different experiments on buoyancy driven mixing processes by means of CFD, Annals of Nuclear Energy 93 (2016) 50–57. doi:10.1016/j.anucene.2015.12.032.

[6] D. Bestion, R. Camy, S. Gupta, C. Heib, O. Marfaing, F. Moretti, T. Skorek, Requirements for cfd-grade experiments for nuclear reactor thermal-

hydraulics, in: CFD4NRS: Computational Fluid Dynamics for Nuclear Reactor Safety, Shanghai, China, 2019.

[7] B. L. Smith, The difference between traditional experiments and CFD validation benchmark experiments, Nuclear Engineering and Design 312 (2017) 42–47. doi:10.1016/j.nucengdes.2016.10.007.

[8] D. Bestion, Review of Uncertainty Methods for Computational Fluid Dynamics Application to Nuclear Reactor Thermal Hydraulics, Tech. Rep. February, OECD/NEA/CSNI (2016).

[9] J. Simoneau, J. Champigny, O. Gelineau, Applications of large eddy simulations in nuclear field, Nuclear Engineering and Design 240 (2) (2010) 429–439. doi:10.1016/j.nucengdes.2008.08.018.

[10] M. Freitag, E. Schmidt, Simulation Benchmark Based on THAI - Experiment on Generation and Dissolution of a Light Gas Stratification By Natural Convection, in: NURETH-19, 2022, pp. 1–17.

[11] F. X. Trias, M. Soria, A. Oliva, C. D. Pérez-segarra, Direct numerical simulations of two- and three-dimensional turbulent natural convection flows in a differentially heated cavity of aspect ratio 4, Journal of Fluid Mechanics 586 (2007) 259–293. doi:10.1017/S0022112007006908.

[12] F. X. Trias, A. Gorobets, M. Soria, A. Oliva, Direct numerical simulation of a differentially heated cavity of aspect ratio 4 with Rayleigh numbers up to 1011 - Part I: Numerical methods and time-averaged flow, International Journal of Heat and Mass Transfer 53 (4) (2010) 665–673. doi:10.1016/j.ijheatmasstransfer.2009.10.026.

[13] F. X. Trias, A. Gorobets, M. Soria, A. Oliva, Direct numerical simulation of a differentially heated cavity of aspect ratio 4 with Rayleigh numbers up to 1011 - Part II: Heat transfer and flow dynamics, International Journal of Heat and Mass Transfer 53 (4) (2010) 674–683. doi:10.1016/j.ijheatmasstransfer.2009.10.027.

[14] A. Badillo, R. Kapulla, Uncertainty Quantification in CFD Simulations of Isokinetic Turbulent Mixing Layers, in: NURETH-15, Pisa, Italy, 2013.

[15] J. Fokken, B. Krohn, R. Kapulla, B. Niceno, H.-M. Prasser, A. Badillo, NEA Benchmark Exercise : Computational Fluid Dynamic Prediction and Uncertainty Quantification of a GEMIX Mixing Layer Test, Tech. rep., OECD/NEA/CSNI (2019).

[16] A. Cutrono Rakhimov, D. C. Visser, E. M. Komen, Uncertainty Quantification method for CFD applied to the turbulent mixing of two water layers, Nuclear Engineering and Design 333 (2018) 1–15. doi:10.1016/j.nucengdes.2018.04.004.

[17] A. Cutrono Rakhimov, D. C. Visser, E. M. Komen, Uncertainty Quantification method for CFD applied to the turbulent mixing of two water layers – II: Deterministic Sampling for input uncertainty, Nuclear Engineering and Design 348 (2019) 146–158. doi:10.1016/j.nucengdes.2019.04.016.

[18] A. Cutrono Rakhimov, D. C. Visser, E. M. Komen, Uncertainty Quantification method for CFD validated for turbulent mixing experiments from GEMIX, Nuclear Engineering and Design 358. doi:10.1016/j.nucengdes.2019.110444.

[19] O. P. Le Maître, M. T. Reagan, H. N. Najm, R. G. Ghanem, O. M. Knio, A stochastic projection method for fluid flow. II. Random process, Journal of Computational Physics 181 (1) (2002) 9–44. doi:10.1006/jcph.2002.7104.

[20] O. P. Le Maître, M. T. Reagan, B. Debusschere, H. N. Najm, R. G. Ghanem, O. M. Knio, Natural convection in a closed cavity under stochastic non-boussinesq conditions, SIAM Journal on Scientific Computing 26 (2) (2005) 375–394. doi:10.1137/S1064827503422853.

[21] O. P. Le Maître, O. M. Knio, H. N. Najm, R. G. Ghanem, Uncertainty prop-

agation using Wiener-Haar expansions, Journal of Computational Physics 197 (1) (2004) 28–57. doi:10.1016/j.jcp.2003.11.033.

[22] J. de Baar, S. Roberts, R. Dwight, B. Mallol, Uncertainty quantification for a sailing yacht hull, using multi-fidelity kriging, Computers and Fluids 123 (2015) 185–201. doi:10.1016/j.compfluid.2015.10.004.

[23] J. H. S. de Baar, Z. Leylek, A. J. Neely, Efficient uncertainty quantification for an axial compressor, using adaptive multi-fidelity Kriging, Proceedings of the 27th ISABE Conference.

[24] P. S. Palar, K. Shimoyama, Multi-fidelity uncertainty analysis in CFD using hierarchical Kriging, 35th AIAA Applied Aerodynamics Conference, 2017doi:10.2514/6.2017-3261.

[25] A. Mohammadi-Ahmar, A. Mohammadi, M. Raisee, Efficient uncertainty quantification of turbine blade leading edge film cooling using bi-fidelity combination of compressed sensing and Kriging, International Journal of Heat and Mass Transfer 162. doi:10.1016/j.ijheatmasstransfer.2020.120360.

[26] A. Mohammadi-Ahmar, M. Raisee, Multi-fidelity uncertainty quantification of film cooling flow under random operational and geometrical conditions, International Journal of Heat and Mass Transfer 152. doi:10.1016/j.ijheatmasstransfer.2020.119548.

[27] X. Huan, C. Safta, Z. P. Vane, G. Lacaze, J. C. Oefelein, H. N. Najm, Uncertainty propagation using conditional random fields in large-eddy simulations of scramjet computations, AIAA Scitech 2019 Forumdoi:10.2514/6.2019-0724.

[28] A. Jivani, X. Huan, C. Safta, B. Y. Zhou, N. R. Gauger, Uncertainty quantification for a turbulent round jet using multifidelity karhunen-loève expansions, AIAA Scitech 2021 Forumdoi:10.2514/6.2021-1367.

[29] P. J. Wenig, R. Ji, S. Kelm, M. Klein, Towards Uncertainty Quantification of LES and URANS for the Buoyancy-Driven Mixing Process between two Miscible Fluids - Differentially Heated Cavity of Aspect Ratio 4, Fluids 6. doi:10.3390/FLUIDS6040161.

[30] F. Nicoud, F. Ducros, Subgrid-scale stress modelling based on the square of the velocity, Flow, Turbulence and Combustion 62 (1999) 183–200. doi:10.1023/A:1009995426001.

[31] F. R. Menter, Two-equation eddy-viscosity turbulence models for engineering applications, AIAA Journal 32 (8) (1994) 1598–1605. doi:10.2514/3.12149.

[32] W. Chung, C. B. Devaud, Buoyancy-corrected k-epsilon models and large eddy simulation applied to a large axisymmetric helium plum, International Journal for Numerical Methods in Fluids 58 (2008) 57–89.

[33] S. Kabelac, M. Kind, H. Martin, D. Mewes, K. Schaber, P. Stephan, VDI-Wärmeatlas, 11. Auflage, 2013.

[34] E. Lemmon, M. McLinden, D. Friend, Thermophysical Properties of Fluid Systems, in: NIST Chemistry WebBook, NIST Standard Reference Database Number 69, National Institute of Standards and Technology, Gaithersburg MD. doi:10.18434/T4D303.

[35] H. G. Weller, G. Tabor, H. Jasak, C. Fureby, A tensorial approach to computational continuum mechanics using object-oriented techniques, Computers in Physics 12 (6) (1998) 620. doi:10.1063/1.168744.

[36] OpenFOAM documentation v2006.

[37] N. Wiener, The Homogeneous Chaos, American Journal of Mathematics 60 (4) (1938) 897–936. doi:10.2307/2371268.

[38] R. G. Ghanem, P. D. Spanos, Stochastic Finite Elements: A Spectral Approach, Springer New York, NY, 1991. doi:10.1007/978-1-4612-3094-6.

[39] R. C. Smith, Uncertainty quantification: Theory, Implementation, and Applications, SIAM, 2014.

[40] B. M. Adams, M. S. Eldred, G. Geraci, R. W. Hooper, J. D. Jakeman, K. A. Maupin, J. A. Monschke, A. A. Rushdi, J. Adam Stephens, L. P. Swiler, T. M. Wildey, W. J. Bohnhoff, K. R. Dalbey, M. S. Ebeida, J. P. Eddy, P. D. Hough, M. Khalil, K. T. Hu, E. M. Ridgway, D. M. Vigil, J. G. Winokur, Dakota, A Multilevel Parallel Object-Oriented Framework for Design Optimization, Parameter Estimation, Uncertainty Quantification, and Sensitivity Analysis: Version 6.10 Theory Manual, Sandia Technical Report SAND2014-4253, May 2019.

[41] J. A. Witteveen, H. Bijl, Modeling arbitrary uncertainties using gram-schmidt polynomial chaos, Collection of Technical Papers - 44th AIAA Aerospace Sciences Meeting 14. doi:10.2514/6.2006-896.

[42] S. A. Smolyak, Quadrature and interpolation formulas for tensor products of certain classes of functions, Dokl. Akad. Nauk SSSR 4 (1963) 240–243.

[43] G. H. Golub, J. H. Welsch, Calculation of Gauss Quadrature Rules, Mathematics of Computation 23 (1969) 221–230. doi:10.2307/2004418.

[44] P. G. Constantine, M. S. Eldred, E. T. Phipps, Sparse pseudospectral approximation method, Computer Methods in Applied Mechanics and Engineering 229-232 (2012) 1–12. doi:10.1016/j.cma.2012.03.019.

[45] B. Adams, W. Bohnhoff, K. Dalbey, M. Ebeida, J. Eddy, M. Eldred, R. Hooper, P. Hough, K. Hu, J. Jakeman, M. Khalil, K. Maupin, J. Monschke, E. Ridgway, A. Rushdi, D. Seidl, J. Stephens, L. Swiler, J. Winokur, Dakota, A Multilevel Parallel Object-Oriented Framework for Design Optimization, Parameter Estimation, Uncertainty Quantification, and Sensitivity Analysis: Version 6.10 User's Manual, Sandia Technical Report SAND2014-4633, May 2019.

[46] K. Karhunen, Über lineare Methoden in der Wahrscheinlichkeitsrechnung, Ann. Acad. Sci. Fennicae. Ser. A. I. Math.-Phys. 37 (1947) 1–79.

[47] M. Loève, Probability theory. Vol. II, 4th ed. Graduate Texts in Mathematics., 4th Edition, Springer New York, 1978.

[48] O. P. Le Maître, O. M. Knio, Spectral Methods for Uncertainty Quantification, Scientific Computation, Springer Dordrecht, 2010. doi:10.1007/978-90-481-3520-2.

[49] C. A. Schenk, G. I. Schuëller, Uncertainty Assessment of Large Finite Element Systems, 1st Edition, Springer Berlin Heidelberg, 2005. doi:10.1007/11673941.

[50] K. Sargsyan, B. Debusschere, H. Najm, O. L. Maître, Spectral Representation and Reduced Order Modeling of the Dynamics of Stochastic Reaction Networks via Adaptive Data Partitioning, SIAM Journal on Scientific Computing 31 (6) (2010) 4395–4421. doi:10.1137/090747932.

[51] B. Peherstorfer, K. Willcox, M. Gunzburger, Survey of multifidelity methods in uncertainty propagation, inference, and optimization, SIAM Review 60 (3) (2018) 550–591. doi:10.1137/16M1082469.

[52] L. W. Ng, M. S. Eldred, Multifidelity uncertainty quantification using non-intrusive polynomial chaos and stochastic collocation, in: Collection of Technical Papers - 53rd AIAA/ASME/ASCE/AHS/ASC Structures, Structural Dynamics and Materials Conference, Honolulu, Hawaii, 2012. doi:10.2514/6.2012-1852.

[53] R. Ghanem, D. Higdon, H. Owhadi, Handbook of uncertainty quantification, Springer Cham, 2017. doi:10.1007/978-3-319-12385-1.

[54] M. Berchier, Multi-fidelity surrogate modelling with polynomial chaos expansions, Master thesis, ETH Zürich (2016).

[55] B. Sudret, A. D. Kiureghian, Stochastic Finite Element Methods and Reliability A State-of-the-Art Report, Tech. rep., University of California, Berkeley (2000).

[56] I. M. Sobol, Global sensitivity indices for nonlinear mathematical models and their Monte Carlo estimates, Mathematics and Computers in Simulation 55 (2001) 271–280. doi:10.1016/S0378-4754(00)00270-6.

[57] B. Sudret, Global sensitivity analysis using polynomial chaos expansions, Reliability Engineering and System Safety 93 (7) (2008) 964–979. doi:10.1016/j.ress.2007.04.002.

[58] A. Saltelli, P. Annoni, I. Azzini, F. Campolongo, M. Ratto, S. Tarantola, Variance based sensitivity analysis of model output. Design and estimator for the total sensitivity index, Computer Physics Communications 181 (2) (2010) 259–270. doi:10.1016/j.cpc.2009.09.018.